

Design and implementation of a novel contact
resistivity measurement method for solar
Si-ZnO:Al contacts.

Bart van Pelt

July 21, 2022

Contents

Introduction	3
I Zinc oxide contacts for solar cells	5
1 Background	6
1.1 Solar cell operation	6
1.2 What is contact resistivity?	10
1.3 Transparency and conductivity	14
2 Methods	16
2.1 Measurements	16
2.1.1 Spectroscopic Ellipsometry	16
2.1.2 Hall effect measurement	16
2.1.3 Contact resistivity	18
2.2 Sample preparation	18
2.2.1 Oxide treatment	19
2.2.2 ZnO:Al ALD process	19
2.2.3 Al ₂ O ₃ capping process	20
2.2.4 Anneal	20
2.2.5 Capping layer etch and silver evaporation	21
3 Results/discussion	24
3.1 Hall/SE	24
3.2 Transmission electron microscopy	28
3.3 Contact resistivity	29
4 Conclusion and outlook	31
II Contact resistivity measurements	32
5 Introduction	33

6	Background	34
6.1	Contact resistivity	34
6.2	Typical measurement methods	35
6.2.1	Cox and Strack	35
6.2.2	Transfer length method	36
6.2.3	Cross bridge Kelvin resistor	38
6.2.4	Pin to plate	41
7	Theory	43
7.1	Transfer length effects	43
7.1.1	Governing equations	44
7.1.2	Uniqueness of solutions	45
7.1.3	Influence of transfer length	46
7.2	Idea: reduce effective sample dimensions	48
8	New approach	52
9	Characterization of measurement method	55
10	Results	57
10.1	Reliability	57
10.2	Validity: Cross Bridge Kelvin Resistor comparison	59
11	Conclusion	61

Introduction

Amidst the ongoing climate and energy crises, solar energy need little introduction. To curb global emissions we need access to efficient, cheap, and reliable energy sources, preferably by yesterday. Broadly speaking, the goal of this work is to find out if cells with aluminium doped zinc oxide (ZnO:Al) front contacts can meet these demands. A general solar cell is illustrated in Figure 1, accompanied with a proposed contact design utilizing ZnO:Al.

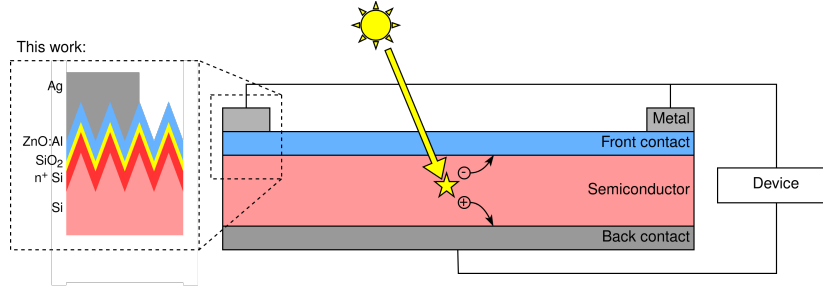


Figure 1: Illustration of a generic solar cell, photons enter the cell through the front contact and generate charge carriers. These charge carriers are collected in the back and front contacts. The box on the left shows the front contact studied in this work, consisting of a textured silicon wafer with an n^+ diffusion zone, covered by a $\text{SiO}_2/\text{ZnO:Al}$ stack. The front metal used here is silver.

Several properties are desired for a good front contact, shortly listed here. A more detailed discussion can be found in Section 1. A high lateral conductivity is needed so that charge carriers can easily reach the metal contacts. The contact should be highly transparent, and provide good optical coupling into the semiconductor bulk. The contact should be *selective*, meaning that it only accepts charge carriers of a particular kind, electrons in our case. Without going into too much detail for now, two parameters need to be low to achieve selectivity: minority carrier recombination and contact resistivity. ZnO:Al has proven itself capable of being transparent and conductive, while showing very little minority carrier recombination. The contact resistivity is the main subject of this work.

Several important process parameters have been studied, such as ZnO:Al doping, the impact of an annealing step, and the silicon doping. It is known

that annealing plays an important role in activating the interface passivation, but what impact does this have on the ZnO:Al itself? Furthermore, previous attempts at creating contacts on intrinsic silicon resulted in high contact resistivities. Can conductive contacts be made by instead using doped silicon? These questions and more are addressed in this thesis. With these results, the main question can be addressed: is ZnO:Al a good front contact material for solar cells? Part I of this thesis shows that this is indeed the case, furthermore, a process window is found in which ZnO:Al provides all of the qualities mentioned above.

The approach taken would seem rather straightforward: ZnO:Al films are deposited, processed further, and then the mentioned material properties are measured. For most material properties, suitable measurement systems were available, however, measuring contact resistivities turned out to be a difficult task. The main obstacle: most etchants etch ZnO:Al too easily to fabricate the test structures usually used to measure contact resistivities. A simple top-down measurement method that had been used previously was found to be very unreliable. To accurately study contact resistivities, a new method had to be found. Part II of this thesis is dedicated to the design and implementation of such a method. The method is a significant improvement of the top-down method which is much more reliable. Compared to conventional methods, a significant advantage is that it can be used for very simple samples, requiring little sample preparation effort.

Beyond the direct scope of this project, being the silicon-ZnO:Al interface, it is worth mentioning potential integration pathways. One of these is currently being explored in the PERCspective project [1] of which the goal is to create a high-quality connection between an industrial PERC cell and a perovskite cell.

Part I

Zinc oxide contacts for solar cells

Chapter 1

Background

1.1 Solar cell operation

Loosely framed the goal of this work is to find out if ZnO:Al passivating contacts can make *good* solar cells. To start answering this question, let's first narrow down what is meant by a *good* solar cell, before diving into the details about contacting layers. The purpose of solar cells is clear: to convert thermal radiation into usable electrical energy. In the ideal case, the incident thermal power, P_{in} , is totally converted to electrochemical power, $V_{\text{out}}I_{\text{out}}$. Thermodynamically, this total conversion is forbidden, the best we can do is to maximize the efficiency,

$$\eta = \frac{V_{\text{out}}I_{\text{out}}}{P_{\text{in}}}. \quad (1.1)$$

Since we cannot control the power output of the sun, this task practically boils down to maximizing the $V_{\text{out}}I_{\text{out}}$ product. Two useful parameters of this current-voltage characteristic are the short circuit current, I_{sc} , and the open circuit voltage, V_{oc} . As I_{out} is a function of V_{out} , these two limiting cases are not enough to know the cells efficiency. To address this a third parameter, the fill factor (FF), is introduced. Ideally, a solar cell would sustain full current output without a decline in output voltage, operating at an output power $V_{\text{out}}I_{\text{out}}$. Realistically though, there is some optimal operating voltage, V_{MP} , at which the cell produces its maximal power, delivering a current I_{MP} . This ratio of *real* output power and *ideal* output power is what defines the fill factor:

$$\text{FF} = \frac{I_{\text{MP}}V_{\text{MP}}}{I_{\text{sc}}V_{\text{oc}}}. \quad (1.2)$$

The fill factor is illustrated in Figure 1.1, where it can be recognized as the ratio between the green and gray surface areas.

In terms of these cell parameters, the efficiency can then be expressed as

$$\eta = \frac{I_{\text{sc}}V_{\text{oc}}\text{FF}}{P_{\text{in}}}. \quad (1.3)$$

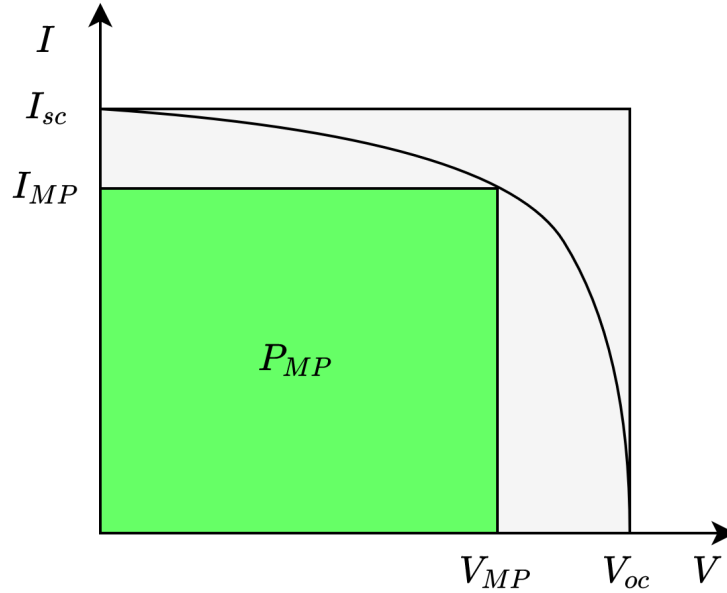


Figure 1.1: Illustration of V_{oc} , I_{sc} and fill factor in relation to a cell's IV-curve. The fill factor can be recognized as the ratio between the areas of the green and gray rectangles.

Measuring these cell parameters requires the fabrication of complete cells. In practice it is more efficient to resort to directly measurable film and contact properties, without relying on the time-consuming fabrication of full devices. Among the desired qualities of a contact are a high transparency, good passivation and a low series resistance. Let's take a look at how these parameters influence the overall solar cell performance.

A typical high school explanation of solar cell operation goes as follows:

1. A photon from the sun is absorbed by the solar cell, here it rips an electron apart from an atom in the crystal, transferring its energy. The electron is negatively charged, but the void it leaves effectively has an opposite charge of equal magnitude, this void is called a "hole".
2. The electron finds its way to one contact of the solar cell, while the hole finds its way to the other.
3. The electron *really* wants to get back to the hole, and the easiest way to do so is to go through the device that you want to power. The electrical energy from the electron is then transferred to the device, providing useful energy.

This rudimentary explanation completely skims over the complex thermodynamical nature of this energy conversion. Moreover it fails to answer basic questions such

as “but why do the electrons and holes move away from each other if they attract each other?” and “okay, so the charges made it to the contacts, why would they not just go back the way they got there instead of taking the whole wire/device detour?”. Despite these and several more shortcomings, this simple model can give us some meaningful heuristic insights into what is needed to make a good front contact. Let’s go through the explanation again, and see what can go wrong with each step.

1. A photons should transfer all of its energy to an electron-hole pair, what if it can’t? This can occur due to several reasons.
 - (a) The photon does not have enough energy to create an electron-hole pair in the base; that is, the photon has an energy below the so-called bandgap of the solar cell’s base.
 - (b) The photon might not even get to the base of the solar cell. If the photon is absorbed in the front contact or reflected by the metal interconnections, its energy is effectively lost. For this reason the front contact should obviously be as transparent as possible.
 - (c) The photon is reflected. If a solar cell reflects a photon back towards the sky, the photon’s energy will not be of much use. A few strategies are used to keep photons trapped in a cell, notably: texturing and antireflection coatings. While light trapping is very important for solar cell efficiency, it will not be further discussed in this thesis.
 - (d) The photon does transfer all of its energy to an electron-hole pair, but the electron-hole pair loses some energy afterwards. This process is called thermalization, by collisions with the crystal atoms the electrons and holes lose energy until they get stuck at an energy similar to the bandgap.
2. Maybe the electron and hole don’t make it to their intended contacts.
 - (a) An electron or hole could reach the wrong contact. In the high-school explanation this sounds very likely, after all, the positive holes should be strongly attracted to the contact that’s filled with negative electrons (and vice versa), right?
 A crucial part to this selectivity is that the contacts should be highly conductive to one type of carrier, while highly resistive to the other. Thus, for n-type contacts a very low electron resistivity should be obtained. A more in-depth discussion of selectivity will be given in Section 1.2.
 - (b) What if the electron and hole don’t even make it to the contacts? It’s possible for the newly formed electron and hole to recombine with each other (or with other electrons and holes), if this happens their electrochemical energy will be lost (of course energy is conserved, but from an engineering perspective it will probably not be useful energy anymore). One possible mechanism for this is radiative recombination,

in which an electron and hole form a photon. This rarely occurs in crystalline silicon due to its indirect bandgap, which means that some additional momentum is needed for this reaction to occur. In crystalline silicon, the most significant recombination pathways are Shockley-Read-Hall (SRH) and Auger recombination. In the SRH mechanism electrons can make small jumps in energy using crystal defects, passing through energy states within the bandgap. These small jumps are more likely to occur than a single large jump. Suppression of SRH recombination is referred to as passivation, and in general this can be achieved by keeping carrier pairs away from defect states. The Auger mechanism is similar to direct radiative recombination, except in this case excess momentum is transferred to a third particle in the vicinity of the recombining carriers.

3. Maybe the generated charges do not transfer their energy to the intended load. This can happen if parasitic series resistances are present in the circuit, as these create potential gradients. In these gradients the electrons lose some useful energy, which cannot be used in the device. For this reason all series resistances should be minimized. This series resistance can be attributed to a few contributions. First, the carriers need to experience a low resistance during transport from the cell bulk to the contact, this is called contact resistivity. Second, once in the contact the carriers should freely flow towards the metal connections, for this a low in-plane resistance is required.

With this oversimplified treatment of solar cell physics, it already becomes clear that highly transparent highly conductive contacting layers are essential for efficient solar cells. Moreover, a high degree of passivation should be achieved so that the generated free charge carriers do not recombine.

Within the PMP group it was found that, in addition to being highly transparent and conductive, ZnO:Al can provide excellent passivation on c-Si [18], a unique combination of properties. A few crucial factors for achieving good passivation were identified. The first is the formation of a high-quality SiO₂ interface between the semiconductor bulk and the ZnO:Al contact, reducing the availability of defects for SRH recombination. Second, available defects can be passivated by hydrogenating them. Keeping hydrogen from effusing out of the contact during annealing is crucial, and this can be achieved by capping the contact with a sacrificial Al₂O₃ layer. While the first two passivating factors rely on creating a defect-free material, the third factor works by keeping carrier pairs away from available surface defects. This so-called field effect passivation can be achieved by doping the ZnO:Al contact, as charged Al dopants repel holes from defects at the interface.

Besides its importance for passivation, the presence of a capping layer was found to be equally crucial for forming high mobility conductive films.

So far, ZnO:Al had shown promising results in passivation, conductivity and transparency, however, attempts to create good contacts on intrinsic silicon were unsuccessful. The focus of this work is to show how high-quality contacts can

be made by instead using doped silicon. These results have contributed to a publication [11] detailing recent work on Si/ZnO:Al contacts within the PMP group.

To do this turned out not to be an easy task, put shortly: measuring contact resistances of ZnO:Al films is difficult to do by conventional methods which often require patterning and etching to create sample structures. The reason being that ZnO:Al is too easily etched by most common etchants, making it difficult to accurately form common testing structures.

Furthermore, contact resistivity measurements require the sacrificial Al_2O_3 capping layers to be fully removed while not keeping the delicate ZnO:Al films intact. To achieve this, a selective etching process was needed. Section 2.2.5 shows how such an etch can be performed with relative ease, achieving a high selectivity.

While the selective removal of Al_2O_3 is shown to be feasible and reliable, still no practical solution was known for forming ZnO:Al testing structures. Due to these metrological difficulties a new measurement method was designed and implemented, which is discussed in detail in the second part of this thesis.

For the first part of this thesis, let's dive into the really interesting question: can ZnO:Al form good solar cell contacts on doped silicon?

As a start we'll rid ourselves of the thusfar handwavy (and dramatically oversimplified) solar cell description so that questions can be framed quantitatively. So far it's only become clear that the contact resistivity should be low, but how is it even defined, and what is low enough? Then the experimental methods will be discussed, including measurements, deposition of the ZnO:Al/ Al_2O_3 stacks, annealing, the removal of the capping layer and subsequent Ag evaporation. Following will be an outline of experimental work on in-plane resistance and transparency, and how different process parameters influence these. This part of the work was done in partial collaboration with Dennis Loeffen, who discussed the electrical and optical properties of ZnO:Al in detail in his masters' thesis [7]. Here these results are treated with less detail, rather focussing on what these results can tell us about which process conditions are needed to obtain low transparencies and low in-plane resistances. Finally, it will be shown that ZnO:Al contacts can have a promisingly low contact resistivity on c-Si, moreover, this can be achieved in a process window in which the other relevant material properties are also excellent.

1.2 What is contact resistivity?

In this section, we will look into solar cell physics in some more detail. For a better understanding, a thermodynamic description of charge carriers in a semiconductor is needed. Semiconductors are defined by having a bandgap, a band of energy values for which no electron state exists. An electron is then either moving around in the conduction band, or bound to an atom while in the valence band. To move between the bands, energy needs to either be supplied to an electron in the valence band, or an electron in the conduction band needs

to somehow get rid of a considerable amount of energy. These generation and recombination processes don't happen instantly, which enables electrons to stay in the conduction band for quite long times. The states within the valence band without an electron are called holes and they can be seen as carrying a positive charge, essentially due to the *absence* of an electron. This property is what distinguishes semiconductors from metals, where electrons are free to decay into lower energy states. For so-called nondegenerate semiconductors, the densities of electrons, n , and holes, p , can be well described by Boltzmann statistics:

$$n = n_{\text{CB}} \exp\left(-\frac{E_{\text{CB}} - E_{\text{F}_n}}{k_B T}\right); \quad (1.4)$$

$$p = n_{\text{VB}} \exp\left(-\frac{E_{\text{F}_p} - E_{\text{VB}}}{k_B T}\right). \quad (1.5)$$

Here n_{CB} and n_{VB} are the densities of states in respectively the conduction and valence bands, E_{CB} and E_{VB} are the energy bounds of the conduction and valence bands, and E_{F_n} and E_{F_p} are the so called Fermi levels of the electron and hole ensembles. In heavily doped semiconductors, such as the ZnO:Al films used in this work, carriers typically follow Fermi statistics instead of the given Boltzmann statistics, these semiconductors are then called degenerate. For the purposes of this explanation, considering only the somewhat simpler nondegenerate statistics is sufficient.

For thermal equilibrium it can readily be derived that $E_{\text{F}_n} = E_{\text{F}_p}$, but this changes when electron-hole pairs are actively generated. In this non-equilibrium situation, one can ask if Boltzmann statistics can be applied, after all, this is a result in equilibrium thermodynamics. Luckily, it typically takes picoseconds for electrons (or holes) to reach equilibrium among themselves. Meanwhile, the equilibration between conduction and valence bands is much slower, electrons can take up to milliseconds on average to make the transition. This means that electrons can be considered in equilibrium, and so can holes, just not in equilibrium with each other. The excesses in electron and hole densities can be described by an increase in E_{F_n} and a decrease in E_{F_p} , a phenomenon called Fermi level splitting. Due to the absence of a bandgap, the separate equilibration of electrons and holes does not occur in metals.

This implies that in a metal, the carrier statistics can be described by a single Fermi level: $E_{\text{F}} = E_{\text{F}_n} = E_{\text{F}_p}$. So far, the Fermi levels have been interpreted merely as a useful way to parametrize the carrier distributions, but they carry greater relevance. A more physical interpretation of the Fermi levels is that they correspond, up to sign, to the electrochemical potentials of both carriers, i.e. $E_{\text{F}_n} = \eta_n$, $E_{\text{F}_p} = -\eta_p$. The free energy of an electron-hole pair, which we want to extract, is then given by $\Delta E_{\text{F}} \equiv E_{\text{F}_n} - E_{\text{F}_p}$. An interesting consideration: in the previous chapter recombination was described as categorically bad, the free energy picture gives a more nuanced view. As the free energy of an electron-hole pair is given by the Fermi level splitting, free energy is only lost when recombination occurs in a region with split Fermi levels, such as the bulk of the cell. In a contact, since there is no Fermi level splitting, recombination does not

amount to free energy losses, and is actually necessary since without contact recombination no currents can flow. This picture also gives a more quantitative description of the heuristic “electrons want to move from one side of the cell to the other, transferring energy to the device”. As the carrier statistics are described by only a single Fermi level in the contacts, the goal is to create a Fermi level difference between the two contacts. To see how these contact Fermi levels are related to the split Fermi levels in the bulk of the semiconductor, we can write down the carrier flux densities as follows:

$$J_n = -\frac{\sigma_n}{e} \nabla E_{F_n}, \quad (1.6)$$

$$J_p = \frac{\sigma_p}{e} \nabla E_{F_p}, \quad (1.7)$$

where $\sigma_n = en\mu_n$ and $\sigma_p = ep\mu_p$ are the conductivities of electrons and holes respectively, expressed in terms of the elementary charge and density and mobility of the specific carriers. In the n-type contact, the Fermi level should be as close as possible to E_{F_n} in the bulk. As the Fermi levels need to come together in the metal, a direct consequence is that a strong gradient in E_{F_p} is needed in the contact. This asymmetry between a strong E_{F_p} gradient and an ideally constant E_{F_n} can be achieved through the associated conductivities: the n-type contact should be very conductive to electrons, but very nonconductive to holes. There are multiple ways to achieve this, but in this work we’ll look at a homojunction in which the carrier densities are influenced by doping the bulk.

An additional benefit of contact doping is that it reduces recombination at the contact surface by lowering the minority carrier density. This reduces the SRH recombination rate, but at the same time the increase in majority carrier density can lead to Auger recombination in the highly doped region, so a compromise needs to be made. The recombination current in the contact can be parametrized as [6]

$$J_{\text{rec}} = J_0 \left(\exp \left(\frac{\Delta E_F}{n_d k_B T} \right) - 1 \right), \quad (1.8)$$

where n_d is an ideality factor, typically ranging between 1 and 2, and J_0 is a scaling factor. As a large Fermi splitting is a design goal for solar cells, the most interesting parameter for reducing recombination is J_0 . Somewhat counterintuitively, J_0 mainly impacts cell efficiency not through J_{sc} , but through V_{oc} . This is because at high recombination rates, lower carrier densities and thus less Fermi level splitting are achieved.

To wrap things up a bit, there are essentially two properties that a good passivating n-type contact needs:

High majority carrier conductivity To avoid Ohmic losses, as parametrized by σ_n . In the rest of this thesis the associated *resistivity* is used, defined by $\rho_n \equiv \frac{1}{\sigma_n}$. Note that ρ_n is a *bulk* resistivity. In contrast, the symbol ρ_c will be used for the contact resistivity. This is reflected in the used units, ρ_n is expressed in $\text{m}\Omega\text{cm}$ while ρ_c is given in $\text{m}\Omega\text{cm}^2$.

Low recombination rates As parametrized through J_0 , to enable a high Fermi level splitting.

An acceptable upper limit for contact resistivity can be found by a rough back-of-the-envelope calculation. As the resistive loss power is given by $P_{loss} = \rho_c J^2 A$ and the output power by $P = VJA$, the resistive losses amount to 1% of the total power when $\rho_c > 0.01 \frac{V}{J}$. Taking typical values for a silicon solar cell: $J \approx 44 \text{ mAcm}^{-2}$ and $V \approx 0.5 \text{ V}$, this limit amounts to $\rho_{max} \approx 100 \text{ m}\Omega\text{cm}^2$.

The results of a more detailed analysis, modeling the impact of contact resistivity and J_0 on an otherwise ideal solar cell's efficiency are shown in Figure 1.2, along with some practically attained efficiencies. It can be seen that at contact resistivities below $100 \text{ m}\Omega\text{cm}^2$, the efficiency is mostly determined by recombination, indicating that these contact resistivities can indeed be considered *sufficiently low*.

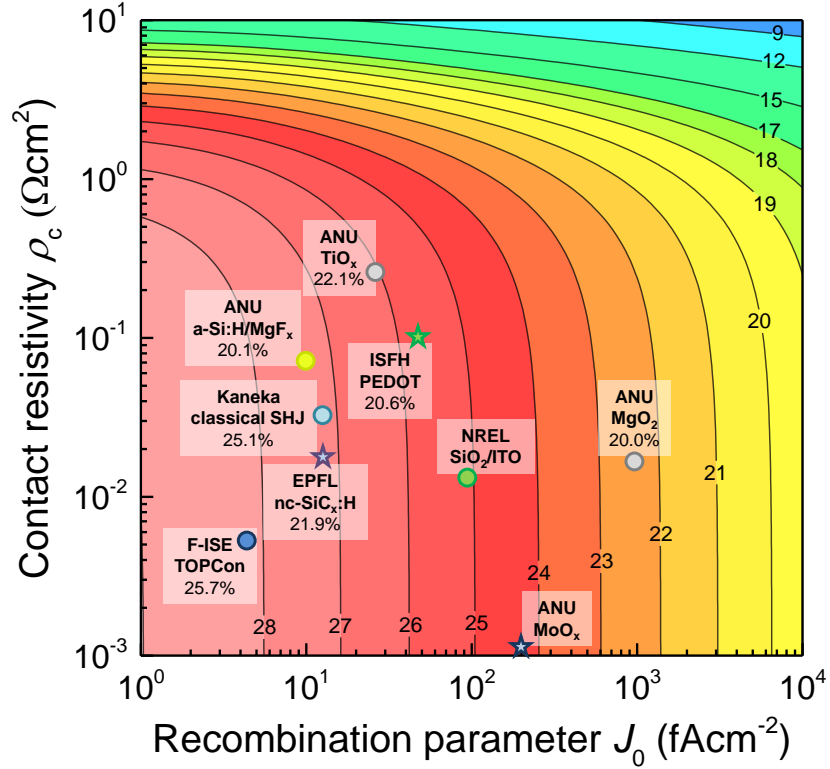


Figure 1.2: Maximum solar cell efficiency as limited by contact resistivity and J_0 , adapted from [12].

In the rest of this thesis, it will be shown that contact resistivities as low as $20 \text{ m}\Omega\text{cm}^2$ can be obtained between ZnO:Al and doped silicon.

1.3 Transparency and conductivity

Before diving into contact resistivities, let's first look at what is required to make the ZnO:Al films transparent and conductive, conductivity here implying in-plane conductivity. The bulk conductivity of an n-type conductor can be described in terms of its carrier density and carrier mobility,

$$\sigma = e\mu_n n, \quad (1.9)$$

to reach a high conductivity, obviously the mobility and carrier densities should be maximized. Reaching a high carrier density can be rather straightforward, simply dope the material strongly. However, high carrier densities also result in increased free carrier absorption, making the material less transparent. This can be quantified by a Drude absorption model, for which the complex dielectric function is given by

$$\varepsilon(\omega) = -\frac{\omega_p^2}{\omega^2 - i\omega\omega_\tau}. \quad (1.10)$$

Here ω_p is the so called plasma frequency, which essentially is the maximum frequency at which the carriers can follow an external field, is given as

$$\omega_p = \sqrt{\frac{e^2 n}{\varepsilon_0 m^*}}. \quad (1.11)$$

The material will be mostly transparent to frequencies above the plasma frequency. The parameter ω_τ is called the scattering frequency, and it broadens the onset of photon absorption, so that photons with $\omega > \omega_p$ can be absorbed as well, it is given as

$$\omega_\tau = \frac{e}{m^* \mu_o}, \quad (1.12)$$

where μ_o is the *optical mobility* of the material. The influence of these two parameters on the optical properties is illustrated in Figure 1.3, the plasma frequency determines the onset of the low energy absorption, while the scattering frequency broadens this absorption front.

It is clear that for high transparency, both ω_p and ω_τ should ideally be minimized. Note that the plasma frequency increases with the carrier density, which conflicts with the high carrier density required from conductivity. More straightforward is the role of the mobility, which increases conductivity and decreases the scattering frequency, making high mobilities very important for transparent conductive materials.

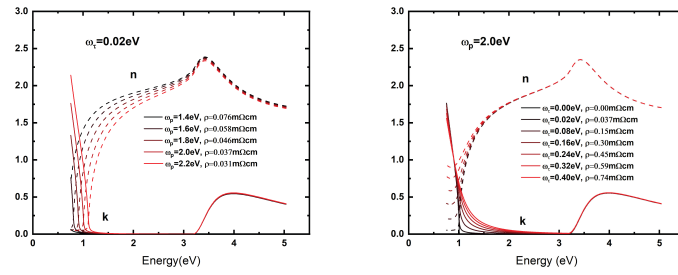


Figure 1.3: Modeled impact of plasma frequency (left) and scattering frequency (right) on the optical properties of ZnO:Al. For realism, bandgap absorption is also shown at the higher energies. Adapted from [7].

Chapter 2

Methods

2.1 Measurements

2.1.1 Spectroscopic Ellipsometry

Spectroscopic ellipsometry (SE) is a method that is often used for measuring a myriad of thin film properties. The method is a form of spectroreflectometry, in which not just the amplitude but also the polarization angle of reflected light is measured. While no direct measurements can be performed, optical models involving material properties, thicknesses, and other parameters, can be fit to the measured spectra. The SE methodology has been described in detail in the MSc thesis of Dennis Loeffen [7] and the already published paper [11].

In this work, SE was mainly used to determine layer thicknesses and free carrier absorption in the ZnO:Al films. Here, free carrier absorption is modeled with a Drude model, parametrized by the frequencies ω_p and ω_τ which were discussed in Section 1.3. Absorption at higher frequencies is modeled using a Tauc-Lorentz model. Layer thicknesses were typically measured with a Woollam variable angle spectroscopic reflectometer (VASE) as measuring at multiple angles makes layer thicknesses easier to fit. However, the used VASE is insensitive in the near infrared range which is relevant to free carrier absorption, so for these measurements a Woollam NIR-SE was used at a fixed angle.

2.1.2 Hall effect measurement

Hall effect measurements can be used to determine in-plane electrical properties of thin films, such as sheet resistance and sheet carrier density. When combined with a film thickness measurement, SE in this work, the more familiar bulk resistivity and bulk carrier density can be calculated. When a magnetic field is applied to a sample conducting a current, the moving charge carriers experience a Lorentz force,

$$\vec{F} = q(\vec{E} + \vec{v} \times \vec{B}). \quad (2.1)$$

As the currents are confined to the sample, a counteracting electric field is formed, so that the Lorentz force equilibrates to net zero. While the electric field itself cannot be measured directly, a Hall voltage can be measured between two points on the sample's perimeter. It can be derived[19] that this induced Hall voltage is independent of the probe positions, as long as the driven current fully passes between the two probes. Furthermore, this measured voltage is found to be equal to

$$V_H = \frac{IB_{\perp}}{nqt} \equiv \frac{R_H}{t}IB_{\perp}, \quad (2.2)$$

where the Hall coefficient R_H is defined as $\frac{1}{nq}$. Since the total current, I , magnetic field magnitude, B_{\perp} and film thickness, t , can be experimentally controlled, the Hall coefficient can be measured. By itself the Hall measurement merely measures the carrier density and type, but when the samples' resistivity, ρ , is also measured, the carrier mobility can also be found by

$$\mu_H = \frac{R_H}{\rho}. \quad (2.3)$$

In this work, Hall effect measurements were all preceded by a resistivity measurement, and the term "Hall effect measurement" will informally refer to this combined measurement. Important to note is that the mobility measured by the Hall method can differ from the mobility measured by SE. A key difference between the two methods is that while in Hall measurements carriers flow through large sections of the sample, in SE incident photons only cause high-frequency local oscillation of carriers. As a result, effects such as grain boundary scattering can significantly impede the movement of carriers in Hall measurements, while locally oscillating carriers might not even come near such grain boundaries. To clarify this distinction the Hall mobilities and optical mobilities will be denoted as μ_H and μ_o in this work.

In this work, Hall measurements were performed using a LakeShore 8400 Series system, using a van der Pauw geometry. A magnetic field of 1T was applied, which is the maximum field strength of the setup. The current ranges for measuring required some fine tuning, with too little current no significant Hall voltages could be measured, while a too high current setting can result in the current source reaching its compliance voltage. As the resistivity and carrier density can vary by several orders of magnitude, this current tuning ended up taking some trial and error. To electrically isolate the ZnO:Al films from the substrate, substrates with a top layer of 450nm SiO₂ were used. On some of the samples, an Al₂O₃ capping layer was present, this caused no issues as the capping layer can easily be pierced by the probe pins of the Hall setup, sometimes requiring gentle pressure. Since the van der Pauw geometry uses four-point probing, the contact resistance between the probe pins and the ZnO:Al films is irrelevant, but care was taken to ensure that the contacts behave Ohmically, as non-Ohmic behaviour can indicate an improper contact.

2.1.3 Contact resistivity

The main contribution of this work is the measurements of contact resistivities of ZnO:Al on doped silicon. These measurements proved very challenging, and this resulted in the design and implementation of a novel contact resistivity measurement. A full discussion of this method is given in Part 2 of this thesis. Typical contact resistivity measurements involve controlled patterning and etching steps to achieve a certain contact geometry. While this can be done with relative ease for some materials, using standard semiconductor fabrication processes, controlled etching of ZnO:Al has previously proved itself challenging, due to its high etch rate in most common etchants. For this reason, typical measurements methods such as the Cox and Strack method (C&S) and the transfer length method (TLM), were not fit for use at the start of this project. Instead, a simple top-down method was used, in which a current is driven through the contact, and the resulting voltage is measured. Sadly, this method proved highly unreliable, mainly due to the inhomogeneities in the driven current distributions. It was found that through more careful electrode design, many of the problems associated with the top-down measurements could be managed. For this, printed circuit boards were designed and used, featuring sets of interleaved copper electrodes. Again, this method is detailed in much more detail in Part 2 of this thesis, but for now, let's focus on the samples that should be used for this method. With the novel method, the interfacial resistance is not actually measured, but instead, the $V(J)$ behaviour of a sample is obtained. Assuming linearity here, the resulting resistivity includes contributions from different materials and interfaces. To give a strict upper bound on the resistivity of the ZnO:Al-Si interface, the other contributions need to be minimized. As the Al_2O_3 capping layer is very resistive, it thus needs to be removed prior to the measurements. For this purpose, a selective wet etch process was used, which will be discussed in more detail later. Important is that this selective etch only needs to fully remove the Al_2O_3 capping layer while leaving the ZnO:Al layer intact. Doing this is much easier than patterned etching.

2.2 Sample preparation

In this work two distinct sample types were used, both shown in Figure 2.1.

The first type, type 1, consists of a polished silicon wafer with a 450 nm SiO_2 top layer. On this, ZnO:Al is deposited, optionally followed by an Al_2O_3 capping layer. The SiO_2 provides electrical insulation between the ZnO:Al and the substrate, so that in Hall measurements all current flows through the ZnO:Al films. Due to their flatness, these samples were also used in the transparency studies, as they give a clean SE signal. The other type, type 2, are symmetric samples which were initially used for passivation studies and then adapted for contact resistivity measurements. These samples consist of a substrate of silicon with an n+ doping profile of either $130\Omega\Box$ or $260\Omega\Box$ on both sides. As is common in solar cell applications, the used substrates were KOH-

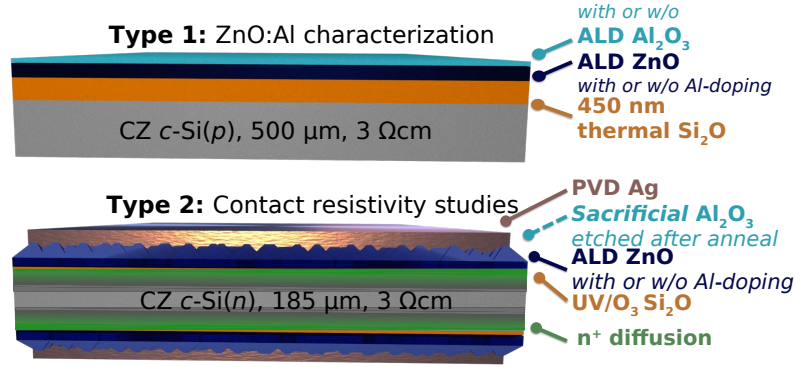


Figure 2.1: Illustration of the two types of samples used in this work.

textured, resulting in a surface of random pyramids. The native SiO_2 top layer was etched away and replaced by a new oxide layer by a UV-ozone treatment. Then, the $\text{ZnO:Al}/\text{Al}_2\text{O}_3$ stack was deposited using the ALD process described below. After deposition on one side of the sample, the samples were flipped and the deposition process was repeated for the other side. After annealing, the passivation of the deposited stacks was studied, more details about this work on passivation can be found in the published paper [11]. After the passivation studies, the Al_2O_3 capping layer is selectively etched, and a contact layer of 300 nm silver is deposited by e-beam evaporation to prepare the samples for contact resistivity measurements. In the following sections the process steps will be discussed in more detail.

2.2.1 Oxide treatment

The type 2 samples received a 1 minute etch in a 1% HF solution to remove the native SiO_2 . After this, a new oxide layer was formed by a 30 minute UV-ozone treatment in a Novascan PSD Series UV Ozone Cleaner.

2.2.2 ZnO:Al ALD process

The ZnO:Al deposition process is the same in both sample preparations. ZnO:Al was deposited by ALD using an Oxford Instruments OpAL tool at a temperature of 200°C . The films are deposited using diethylzinc (DEZ) and dimethylaluminium isopropoxide (DMAI) in a supercycle process, with water used as a coreactant. The Al content can be controlled using the number of DEZ cycles per DMAI cycles, which is called the cycle ratio, with for example r16 meaning 16 DEZ cycles per DMAI cycle. An exception to this naming scheme is intrinsic ZnO , in which no DMAI cycles are used, this is denoted as int. Note that a high cycle ratio implies a low Al doping. The used dopings used in this work were int, r96, r48, r24, r16. The order of the cycles is chosen so that the dopant cycles

are evenly spaced, and not at the top or bottom of the film. r16 then implies 8 cycles of DEZ, 1 cycle of DMAI, followed by 8 cycles DEZ. This supercycle can then be repeated to obtain the desired film thickness. The used supercycle is illustrated in Figure 2.2.

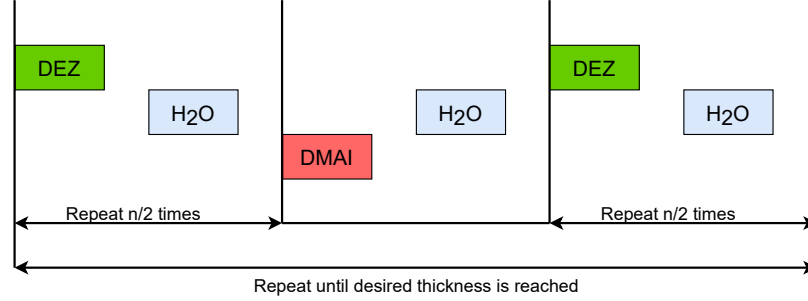


Figure 2.2: Illustration of the supercycle used to deposit ZnO:Al films, here n denotes the cycle ratio. Not explicitly shown are the purge steps between the dosing steps.

2.2.3 Al₂O₃ capping process

On some samples a 30nm Al₂O₃ capping layer was deposited by ALD, this was also done in the OpAL reactor, using only DMAI and water as precursors, again at 200°C. To deposit capped and uncapped type 1 samples efficiently, the uncapped samples were removed from the reactor after ZnO:Al deposition. After this, the remaining samples received the Al₂O₃ capping layer. As it became clear that capping is absolutely crucial to obtain good material properties, all type 2 samples were capped. While fabricating these type 2 samples the process was not interrupted between the ZnO:Al and Al₂O₃ depositions.

2.2.4 Anneal

Type 1 samples were successively annealed so that a single sample could be reused at different anneal temperatures. As a check, pieces of capped r24 ZnO:Al were annealed directly to the intended temperature, here little deviation could be found from the successive annealing. Annealing was performed in steps of 50°C, starting at 300°C. To be able to perform the annealing steps quickly in between measurements, the anneals up to 500°C were performed on a hotplate, as the used hotplate has a maximum temperature of 500°C. Here a carrier wafer was used to support the samples, which was put on the hotplate and removed after 5 minutes, allowing the samples to cool down again. Anneals at temperatures higher than 500°C were performed in a Jipelec Rapid Thermal Annealer (RTA). The type 2 samples were directly annealed to the right temperature in the RTA.

2.2.5 Capping layer etch and silver evaporation

To prepare the type 2 samples for contact resistivity measurements, the Al_2O_3 capping layer needs to be removed without destroying the ZnO:Al film. A selective wet etch was adapted from [17], using a solution of Na_2CO_3 and KOH, at a temperature of 60°C and a pH of 11.

To verify that this etching process works as intended, film thicknesses were measured with SE before and after etching. This run was performed on as-deposited r24 ZnO:Al + Al_2O_3 samples, with etching times ranging between 30 seconds and 5 minutes. The results are illustrated in Figure 2.3, where the ZnO:Al and Al_2O_3 thicknesses are shown as a stack, the error bars indicate the surface roughness as determined by SE. Shown on the left are the film stacks before the etching process, these all appear very similar in thicknesses. Shown on the right are the same samples, but after being etched at the indicated etching times.

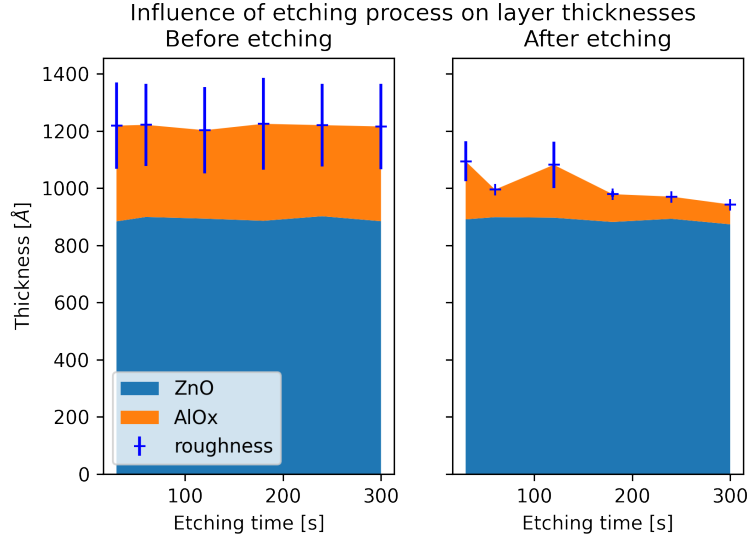


Figure 2.3: Cumulative thicknesses of deposited films before and after etching, as measured by SE.

As visible, the Al_2O_3 thickness significantly decreases for even 30s etches, furthermore, the decrease in thickness saturates, indicating that no more material is being etched after around 3 minutes. Still, the SE measurements appear to indicate that some Al_2O_3 remains. Further inspection of the performed fits however shows that the Al_2O_3 and ZnO:Al thickness are strongly inversely correlated. This indicates that the apparent remaining Al_2O_3 is a mere fitting artefact. Since the total ZnO:Al + Al_2O_3 thickness does not decrease after around 3 minutes, it is assumed that the etching process indeed stops when it reaches the ZnO:Al film. Full removal of the Al_2O_3 film was verified using a Si/ Al_2O_3 sample, on which no Al_2O_3 could be found by SE after etching.

Looking only at the initial measurements, in which SE could more clearly distinguish between the ZnO:Al and Al₂O₃ films, the etch rate is estimated at around 4 Å per second.

Less quantitative, but perhaps more convincing, evidence for the efficacy of the etch process was accidentally found in a TEM study on a contact resistivity sample. This sample was annealed at 500°C, etched for two minutes, and then coated with silver.

Here, instead of the expected Si/ZnO:Al/Ag stack, a Si/ZnO:Al/Al₂O₃/ZnO:Al/Ag stack was found. The reason for this is the backside deposition of the ALD films, resulting in a ZnO:Al/Al₂O₃/ZnO:Al/Al₂O₃ stack being deposited around the edges of the sample. While this backside deposition was unintended, the TEM image in Figure 2.4 clearly shows a full removal of the top Al₂O₃ layer, while the top ZnO:Al layer did not significantly reduce in thickness.

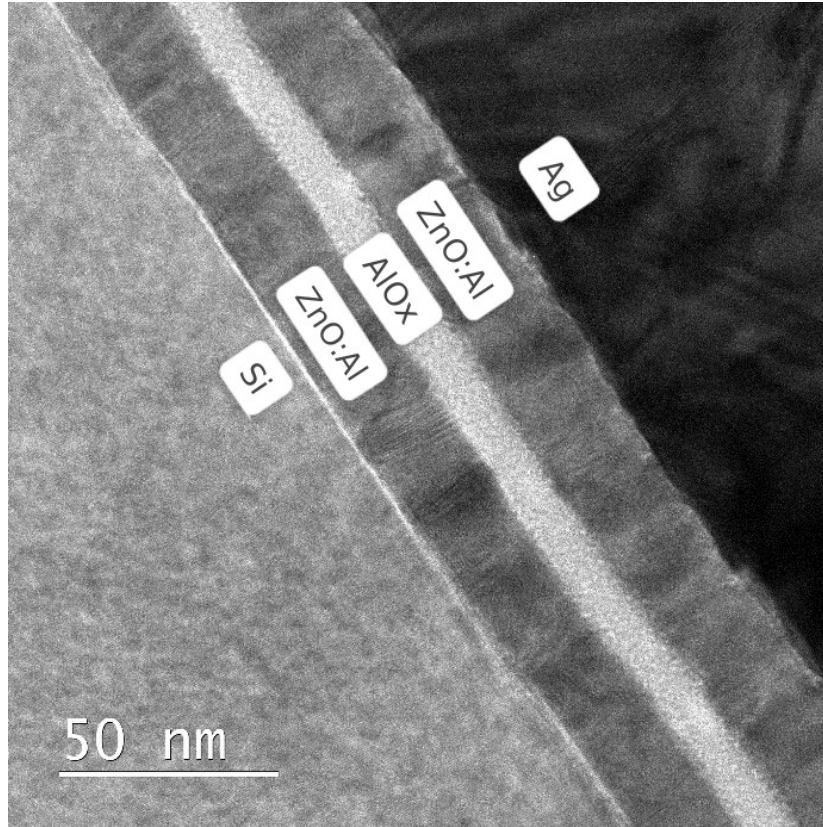


Figure 2.4: TEM image of a sample with unintended background deposition, after removal of the top Al₂O₃ layer and silver evaporation.

This combination of estimated etch rate and TEM imagery motivated the decision to etch all samples for a duration of 2 minutes.

After the removal of the capping layer, the type 2 samples were covered with

300 nm of silver by e-beam evaporation. To effectively remove the backside deposited regions, it was found useful to mildly scratch these visually recognizable regions before silver evaporation. After evaporation, the color differences between the ZnO:Al and ZnO:Al/Al₂O₃/ZnO:Al coated regions could of course not be seen, but the scratches remained visible after deposition. Good samples could then be cleaved from the non-scratched region of the wafer.

Chapter 3

Results/discussion

3.1 Hall/SE

We start by looking at the bulk resistivity, carrier density and carrier mobility of ZnO:Al films, shown in Figure 3.1. Immediately clear is that doping the ZnO can lower the bulk resistivity by an order of magnitude. This decrease in resistivity can be attributed to an increasing carrier density, as the Hall mobility decreases with doping. In the as-deposited state, the capped and uncapped samples show similar properties.

Next, let's look at the impact of an annealing treatment. Here, a clear difference is found between the capped and uncapped samples. Uncapped samples become more resistive by several orders of magnitude upon even mild anneals, while capped samples show much more stable behaviour. This shows that the presence of a capping layer is crucial for achieving a high film conductivity.

Focusing our attention to the capped samples, the annealing step results in a reduction of resistivity, in some samples up to 50% compared to as-deposited. For the doped samples a minimum in resistivity is reached around 550°C to 650°C, after which an increase is found at 700°C anneals. Interestingly, this increase in resistivity at the highest anneal temperatures is not seen in intrinsic ZnO.

The deterioration of uncapped films can be attributed to a decrease in both carrier density and Hall mobility. The decrease in resistivity with doping is found to be attributed to the increased carrier density only, as overall the Hall mobility decreases with doping level. This decrease in Hall mobility is likely to be caused by increased impurity scattering on Al dopants. For capped samples, annealing at temperatures above 500°C results in an increased Hall mobility and carrier density. This is potentially caused by an activation of the Al dopants by diffusion. This diffusion will be discussed in more detail in Section 3.2 about the TEM studies performed within this project.

Next, let's look at the transparency of the produced films, now focusing only on the capped samples.

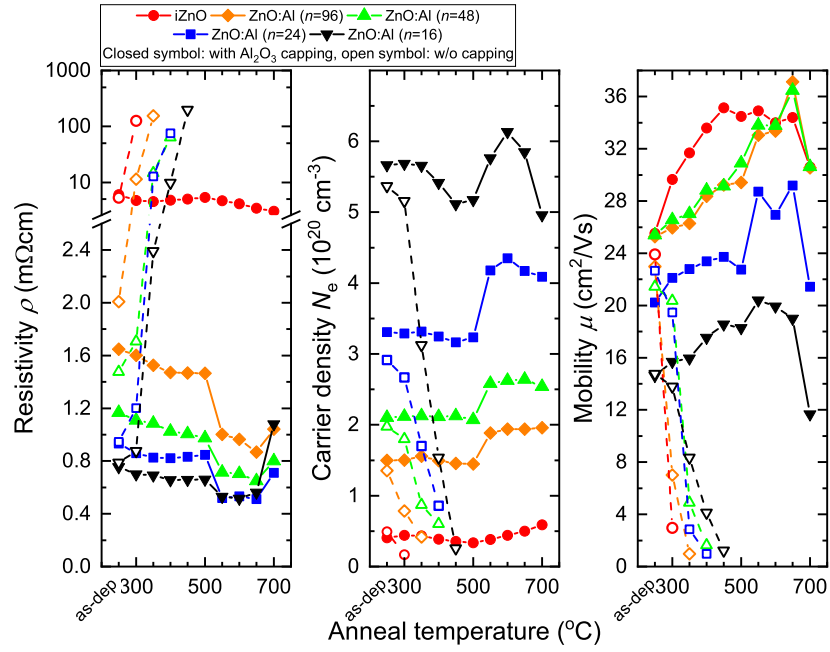


Figure 3.1: ZnO:Al bulk resistivity, carrier density and carrier mobility, depending on doping level, capping and annealing temperature. A strong degradation is seen when annealing uncapped samples, indicating that the capping step is crucial. The resistivity decreases with doping level. During annealing of capped samples the resistivity decreases significantly, in some cases being half as resistive as the as-deposited films.

The measured plasma and scattering frequencies are shown in Figure 3.2. As expected, the plasma frequency strongly depends on the doping level. Furthermore, the plasma frequency increases in the 550°C to 650°C annealing temperature range, and decreases after a 700°C anneal. These trends are similar to the trends in carrier density found by Hall measurements.

In doped ZnO the scatter frequency monotonically decreases strongly with annealing temperature. In the (n96, n48, n24) doping levels the scattering frequency increases slightly with doping level. When increasing the doping level to n16, the scattering frequency surprisingly decreases.

To quantify the impact of these parameters on cell performance, J_{sc} can be estimated from the measured optical constants of the ZnO:Al films. This optical modeling was performed using the PVLighthouse OPAL2 calculator [13]. These results are shown on the right of Figure 3.2, details on these simulations can be found in [7, 11]. Overall, J_{sc} decreases with doping and increases with annealing temperature. From a pure optical point of view, this implies that lowly doped ZnO:Al should be used, which is annealed to very high temperatures. This contrasts with the electronic point of view, where sufficient doping is needed to achieve a low resistivity.

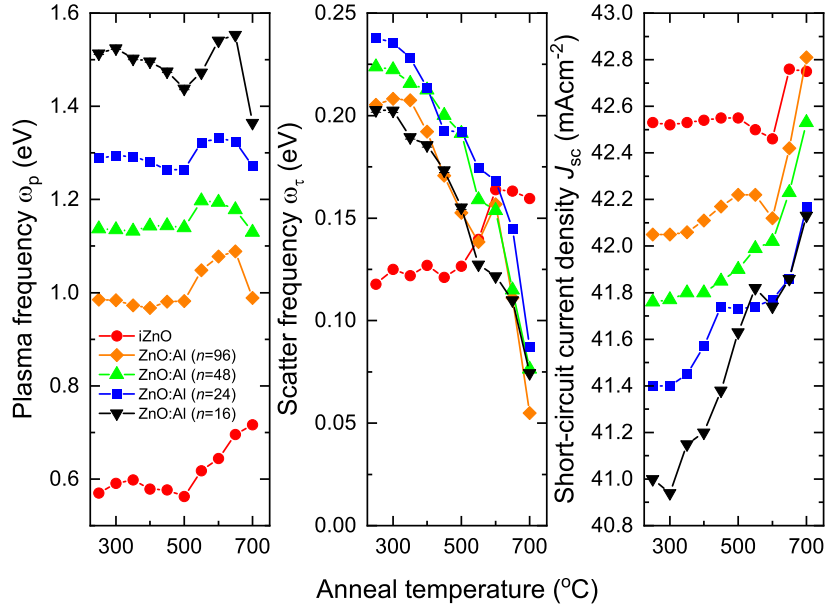


Figure 3.2: Measured plasma and scattering frequencies of capped samples (left and middle), simulated J_{sc} (right). Dependent on ZnO:Al doping level and annealing temperature.

To put the optical and electronic properties in context, Figure 3.3 shows the measured conductivities and simulated J_{sc} values. Also shown are literature values of several competing materials. It can be seen that ZnO:Al can attain optical and electrical performance similar to IZO and IT O. This is very promising,

as zinc is much more abundant than the indium needed for these typically used TCO's.

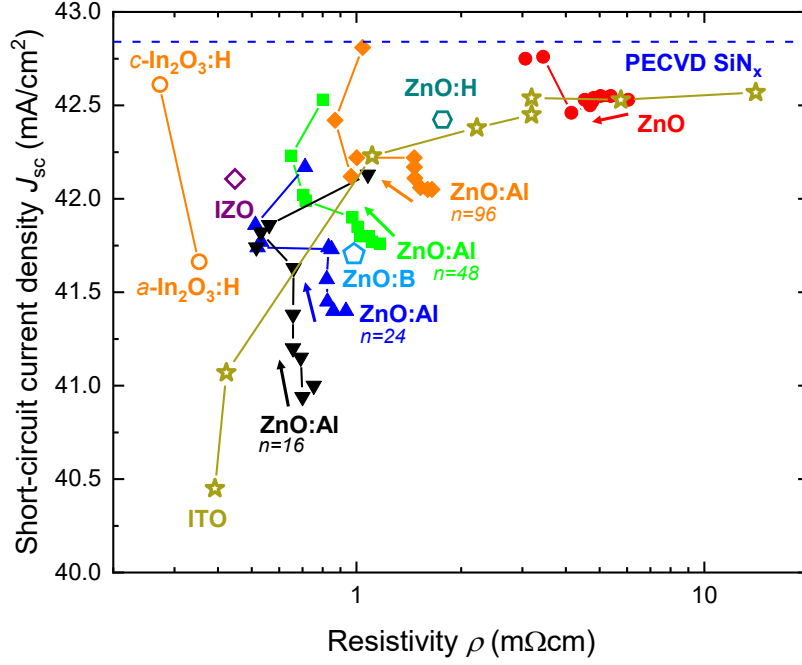


Figure 3.3: Overview of measured ZnO:Al bulk resistivity and simulated J_{sc} values. Arrows indicate increasing anneal temperatures. For comparison, datapoints of PECVD SiN_x, PVD ITO, PVD IZO, ALD ZnO:B, ALD ZnO:H and amorphous and crystalline In₂O₃:H are shown. Adapted from [11].

While Figure 3.3 provides clear motivation for using ZnO:Al contacts, a few key details are omitted. Besides transparency and lateral conductivity, we also have to consider the passivation and contact resistivity of these films. In previous work, the passivation is found to degrade significantly at annealing temperatures above 500°C [11].

The remaining step is to find out if low contact resistivities can also be attained. Combining the passivation requirements with the lessons from Figure 3.3, the decision was made to focus on lowly doped ZnO:Al annealed at temperatures of 400°C and 500°.

Before looking into contact resistivities, the next section discussed TEM results, as these may shed some light into what happens during the annealing steps.

3.2 Transmission electron microscopy

To gain more insight into how annealing impacts the ZnO:Al properties, some samples were analyzed by transmission electron microscopy (TEM). As the Hall and SE measurements indicate some interesting differences between the anneals at 400°C and 600°C, these conditions were chosen for further investigation. Both samples were capped during the anneal, and both contained r48 ZnO:Al. HAADF-STEM (High-Angle Annular Dark-Field) images of both samples are shown in Figure 3.4. In the 400°C sample the capping layer was etched away, followed by silver deposition. As the silver was found to diffuse into the sample, the choice was made to keep the capping layer intact on the 600°C sample.

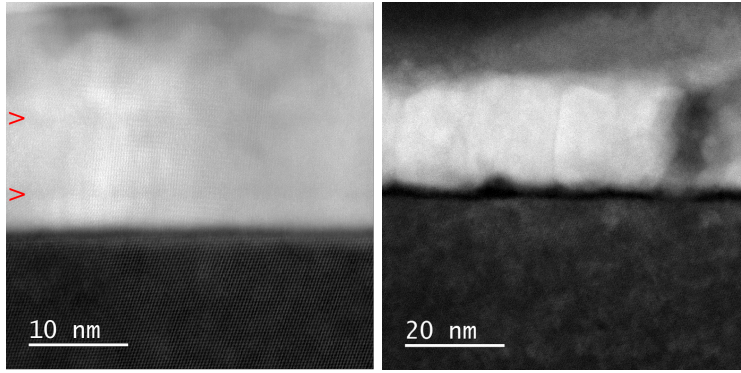


Figure 3.4: Comparison between r48 ZnO:Al annealed at 400°C (left) and 600°C (right). In the 400°C sample the Al_2O_3 capping layer was removed, followed by Ag evaporation. In the 600°C the Al_2O_3 capping layer was not removed. Note the presence of two faint dopant lines in the 400°C sample.

In this TEM variant elements with high atomic mass appear brighter. The lower dark section of each image corresponds to the silicon wafer, covered by a brighter ZnO film. As mentioned before, the diffusion of Al dopants was expected to play a role in the increased carrier densities at high annealing temperatures, as these dopants become more active when spread out. In the 400°C sample, Al dopant planes can be seen as faint lines, indicating that no diffusion had taken place. In the 600°C sample, these dopant planes could not be discerned anymore, indicating a possible diffusion of dopants.

Besides dopant dispersion, a clear difference in crystal structure can be seen between the samples. After annealing at 600°C, crystals grains are easily distinguished from each other, indicating significant growth and grain coarsening. The 600°C film also looks much rougher, and voids in the ZnO:Al film can be seen as darker spots. Overall, the grain coarsening appears to increase the Hall mobility, as the influence of grain boundaries is decreased.

3.3 Contact resistivity

Finally, we look at the contact resistivities of ZnO:Al on n^+ diffused silicon. Recall that on intrinsic silicon, no good contacts could be created, is this different on doped silicon? Luckily, this is the case, Figure 3.5 shows measured contact resistivities as low as $20 \text{ m}\Omega\text{cm}^2$! This is well below the device fitness goal of $100 \text{ m}\Omega\text{cm}^2$. Previously obtained passivation results indicated that reaching $J_0 \lesssim 100 \text{ fA/cm}^2$ is well feasible [11]. Combined with these new contact resistivity results, Figure 1.2 shows that ZnO:Al contacts perform similarly to other state-of-the-art contacts.

A few important behaviours can be found. First, ZnO:Al doping is crucial and it can decrease the contact resistivity by over an order of magnitude. Interestingly, stronger ZnO:Al doping is not necessarily beneficial, as on $260 \text{ }\Omega\Box n^+ \text{ Si}$, r48 doped ZnO:Al produces more resistive contacts than r96 ZnO:Al. A possible explanation for this effect is the distance of the first Al doping layer from the interface. In strongly doped ZnO:Al this layer is relatively close to the interface, as ZnO initially grows in islands, there is a possibility of depositing Al_2O_3 directly on the SiO_2 if the ZnO islands do not yet fully cover the interface.

Next, let's consider the impact of the annealing temperature on contact resistivity. Focusing on samples with doped ZnO:Al, annealing at 500°C can be seen to increase contact resistivity when compared to a milder anneal of 400°C . This trend is opposed in intrinsic ZnO samples, for which the resistivity decreases slightly in this range. The mechanism for this is not precisely known, but it is hypothesized to be caused by diffusion of Al within the ZnO:Al, based on the following cues. In TEM investigations within this project, it was found that Al was more dispersed after a 500°C anneal than after a 400°C anneal. In another study, accumulation of Al was found to occur in polysilicon-ZnO:Al interfaces. Together, the occurrence of Al diffusion and its apparent tendency to accumulate at interfaces might be the factors contributing to this increased resistivity.

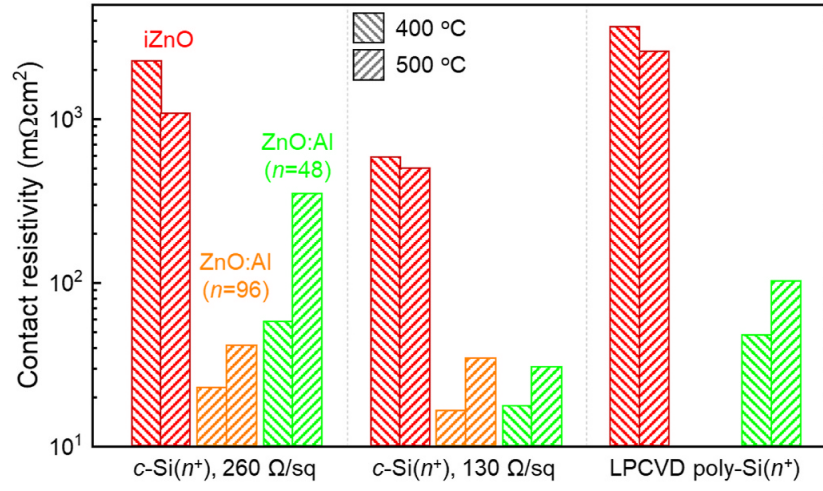


Figure 3.5: Contact resistivities of ZnO:Al on doped silicon. For comparison, contacts on $\text{SiO}_2/\text{poly-Si}(n^+)$ stacks are also shown.

Chapter 4

Conclusion and outlook

The goal of this project was to find out whether ZnO:Al can be used to create high quality front contacts for silicon solar cells. In this work it is shown that an ZnO:Al/Al₂O₃ stack can provide excellent contacts on n+ doped silicon. Luckily, the process conditions needed to achieve this align well with those needed to obtain high quality passivation, conductivity and transparency. It was found that the doping of both the silicon and ZnO:Al is crucial for forming good contacts, and the contact quality decreases for high temperature anneals, with a significant degradation found between 400°C and 500°C anneal temperatures. When combined with the previous passivation studies, this work presents a clear process window in which ZnO:Al films can be made laterally conductive, transparent and passivating while making excellent contacts on n-doped Si. The necessity of a capping layer is shown, furthermore, with mild ZnO:Al doping a high transparency and conductivity can be achieved, both in-plane and as a contact. Annealing should occur around 400°C to 500°C, as in this range the passivation, contact resistivity, ZnO:Al bulk conductivity and transparency are excellent. This means that further research can focus on device integration, something which is already being done in for example the Percspective project, aiming to use ZnO:Al as a full area passivating contact layer.

Part II

Contact resistivity measurements

Chapter 5

Introduction

In the previous part of this thesis, the contact resistivity of Al-doped zinc-oxide on doped silicon was investigated, while omitting details on the performed measurements. In this part of this thesis, the devised measurement setup and method will be described in full detail. The method provides an alternative to typical contact resistivity measurements, in which several processing steps are needed to create accurately shaped contacts on the samples of interest. These methods include the Cox and Strack (C&S) and Transfer Length Method (TLM) methods, which will be explained later. Fabrication of testing structures is especially difficult for ZnO samples, as ZnO etches quickly and irregularly in most common etchants [10, 4]. Essentially, this means that any sample preparation method involving a “carefully etch away a specific piece of ZnO:Al” step is off-limits. Furthermore, even if this were achievable, thermal and chemical processing steps could alter the electrical properties of the contact of interest. After sample preparation there is then no guarantee that the tested contacts accurately resemble the contact as it would behave in a practical device.

At the start of this project a simple measurement method was suggested. Coat a sample with a thin film of silver, drive a current between the top and bottom of this sample and measure the resulting potential difference. Multiplying the obtained resistance by the area of the sample should then give the specific resistance of the sample. While this suggested pin-to-plate measurement is very easy to perform, it quickly became clear that the method was so unreliable that useful data could not be obtained. As the C&S and TLM methods provide some significant challenges, the choice was made to look deeper into the pin-to-plate method, and see if it can be improved on enough to be useful. This work presents a solution to this problem, in which custom printed circuit boards are used to control the current flow in the samples. This method is able to characterize samples without the need of controlled ZnO:Al removal, requiring only a metallization step to ensure good contacts between the probes and the sample.

Chapter 6

Background

6.1 Contact resistivity

In Part 1 of this thesis, contact resistivity was identified as a potential limiting factor for solar cell efficiency. As a consequence, it is important that the contact resistivity is minimized. But first: what does contact resistivity even mean? A total contact resistance can be defined as $R_c = \frac{V}{I}$, with V and I being the voltage along the contact and the total current respectively. This quantity is not really that useful, if you double the area of a contact you should get approximately (more on this later) twice the current at the same voltage, halving the contact resistance. A more useful quantity is the contact resistivity, also known as specific contact resistance, which is area independent. This ρ_c is defined not using the total current, but the current density J :

$$\rho_c = \left. \frac{\partial V}{\partial J} \right|_{V=0}. \quad (6.1)$$

While from a theoretical point of view this description of contacts in terms of $J(V)$ sounds perfectly reasonable, its usage can be challenging in practice. To understand the problem, consider preparing a sample of area A and assuming that the current is uniformly distributed along the contact. The definition then easily translates to $\rho_c = \frac{V}{I}A$, where the total current I and induced voltage V can be measured. In reality, the current distribution into a contact might not be uniform. For example, this can occur due to an effect called current crowding[15]. In current crowding, most of the current flows through a narrow region along the edge of a contact, instead of being evenly spread out. This phenomenon is illustrated in Figure 6.1. The current density decays exponentially with characteristic length $L_t = \sqrt{\frac{\rho_c}{R_\square}}$, called the transfer length, here R_\square is the sheet resistance of the wafer. This effect is analyzed in Section 7.1, where this characteristic transfer length is derived.

This effect will be explained in more detail in Chapter 7, but first, let's think about its experimental implications. If the transfer length is much larger than

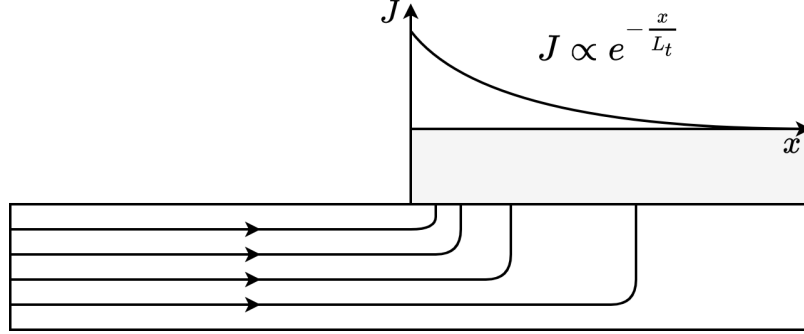


Figure 6.1: Illustration of current crowding along the edge of a contact. The current density J decays exponentially with distance from the contact edge. Shown are a wafer and a contact, current flows into the wafer from the left and into the contact, as indicated by the arrows.

the contacts, then the current will effectively be equally distributed. Sadly, for the samples used in this work, the transfer length was often found to be smaller than the samples' dimensions. In such cases measuring V and J is not trivial, as they can vary greatly within the contact. In contrast to these locally defined V and J , it is typically only the total current, I , and *some* induced voltage, V_M , that can be measured experimentally. This is the main challenge of contact resistivity measurements: reliably distilling local $J(V)$ behaviour from global $I(V_M)$ measurements. In the next sections some typical solutions to this challenge will be discussed. Sadly, most of these methods involve controlled partial etching, which, as discussed, can be extremely difficult for ZnO:Al.

Within the context of this project, symmetric lifetime samples were often made, consisting of a substrate with ZnO:Al deposited on both sides. These are further processed by thermal annealing after deposition of an Al_2O_3 capping layer. As this capped etching step is one of the focuses of this work, it is desirable to not change this process too much for contact resistivity samples. This is the main motivation for this part of this thesis, to figure out a way to quantify the contact resistivity of Si-ZnO:Al contacts using the available lifetime samples, without needing to drastically alter them.

6.2 Typical measurement methods

6.2.1 Cox and Strack

In the Cox and Strack (C&S) method[16] samples are made that feature circular contacts of varying size on one side of the sample, while the other side has a full backplane contact, as illustrated in Figure 6.2.

The resistance between the backplane and the circular contacts is then measured for the different circular contacts. The main assumption here is that the total resistance can be described as a sum of three resistances: contact

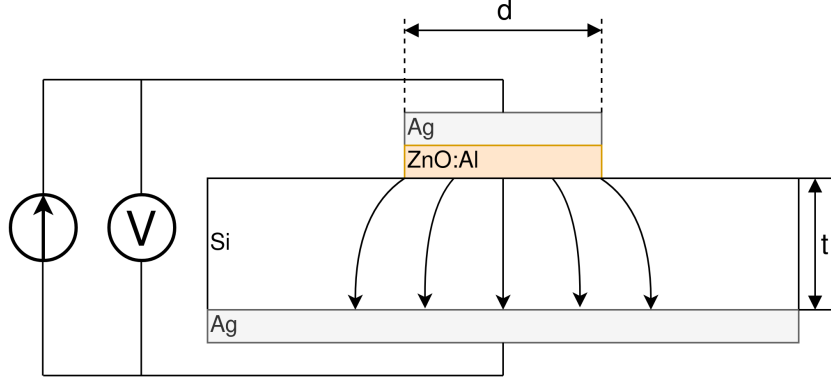


Figure 6.2: Illustration of a Cox and Strack measurement setup, the ZnO:Al and covering Ag layers are circularly shaped with diameter d , the Si and bottom Ag layers are much larger than the circular contact. t indicates the thickness of the Si layer. In practice, a single sample would be covered by multiple dots of varying diameter. The spreading resistance in the silicon scales differently with d than the contact resistance does, so that it can be fit out with sufficient data points.

resistance R_c , spreading resistance R_s , and some fixed residual resistance R_0 . Cox and Strack originally modeled these terms as

$$R_T \approx \underbrace{\frac{\rho_W}{\pi d} \arctan\left(\frac{4t}{d}\right)}_{R_s} + \underbrace{\frac{\rho_c}{\frac{1}{4}\pi d^2}}_{R_c} + R_0, \quad (6.2)$$

where d is the diameter of the contact, ρ_W is the wafer resistivity, ρ_c the contact resistivity and t is the thickness of the wafer [5]. Since the contact and spreading resistances depend differently on the contact radius, the contact resistivity can be determined by varying d and fitting to the model. While more accurate models for the resistance terms in Equation 6.2 have been found [20, 3], the concept behind the measurement stays the same. The practical implications of this method are that samples have to be precisely made, the circular contacts are typically tens of micrometers in radius. To make structures like this one would need to remove most of the ZnO:Al contacting layer, leaving only the circular contacts behind. As discussed previously, this is not practical for ZnO:Al. While it has this major drawback for ZnO:Al contacts, the Cox and Strack is a popular measurement method for solar cell applications. Contact resistivity measurements in the sub-m Ωcm^2 range have been reported [8] using this method.

6.2.2 Transfer length method

The transfer length method (TLM) somewhat resembles the C&S method in the sense that multiple sample geometries are used to fit out the contact resistivity. In TLM, the chosen geometry can be either linear or circular [16], these variants

are conceptually similar, so only the linear variant is discussed here. A linear TLM setup is illustrated in Figure 6.3.

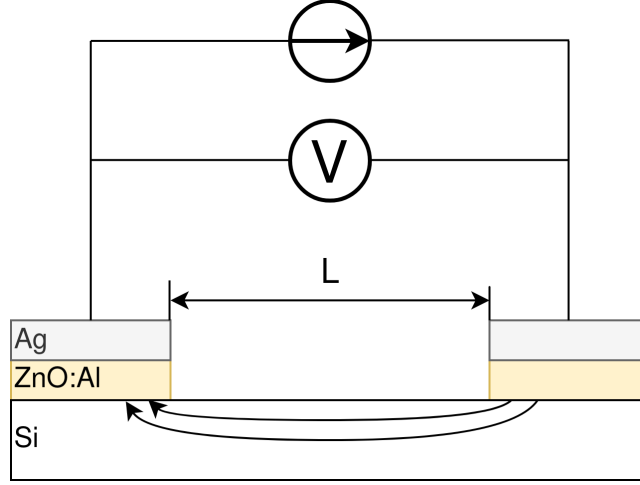


Figure 6.3: Side view illustration of a TLM measurement setup, on a rectangular sample of width W (not shown) several rectangular contacts are made, two shown here. The distance L between the contacts is varied. Note that the current is not uniformly distributed over the contact, but is localized within a transfer length L_t .

In this setup the total resistance consists of twice the contact resistance R_c and the resistance of the Si wafer R_w . The wafer resistance can be expressed as

$$R_w = \frac{LR_{\square}}{W}, \quad (6.3)$$

in which W is the width of the sample and R_{\square} is the sheet resistance of the wafer.

Through current crowding, the currents are effectively localized to within a transfer length $L_t = \sqrt{\frac{\rho_c}{R_{\square}}}$ of the contact edge, this length will be derived in Chapter 7. This current crowding implies that the contact has an effective area of WL_t . Now take for the contact resistance $R_c = \frac{\rho_c}{WL_t} = \frac{R_{\square}L_t}{W}$, where the definition of L_t was used to obtain the second expression. Now the total resistance can be expressed as

$$R_T = 2 \underbrace{\frac{R_{\square}L_t}{W}}_{R_c} + \underbrace{\frac{LR_{\square}}{W}}_{R_w} = \frac{R_{\square}}{W}(2L_t + L). \quad (6.4)$$

Here, the horizontal and vertical intercepts signify twice the transfer length and twice the contact resistance respectively, as shown in Figure 6.4.

After finding the intercepts, the specific contact resistivity can be found as $\rho_c = R_c L_t W$.

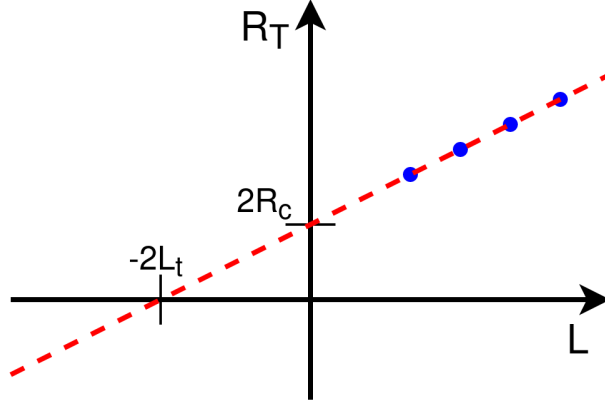


Figure 6.4: Example of a TLM analysis, the red fit line intercepts the horizontal axis at $-2L_t$ and the vertical axis at $2R_c$.

The drawbacks of this method are similar to those of the C&S method, patterning and etching steps are required, making TLM not only difficult, but also possibly undermining the validity of the obtained results. Again, the ZnO:Al film should be partially removed in a controlled way, which is best avoided. A difference with the C&S method is that TLM samples imply symmetric measurements of a contact, in Ohmic contacts this is not an issue, but since in TLM the contacts are always in an antiseriess configuration, this can make non-Ohmic contacts difficult to characterize.

6.2.3 Cross bridge Kelvin resistor

While the previously described methods rely on being able to fit out the contact resistivity from some set of measurements, the cross bridge Kelvin resistor (CBKR) method takes a different approach. In essence the method is a top-down four-terminal measurement. A current is driven from the top to the bottom of a sample using two terminals, while two other terminals are used to measure the resulting voltage. The typical setup is illustrated in Figure 6.5.

The electrodes are formed as two L-shapes, one on either side of the sample, with their “legs” opposed to each other. One set of opposed legs is used to drive the current, while the other opposed set is used to measure the voltage. With this approach parasitic resistances are easily ignored, as the voltage measuring wires carry no current.

Measure the total resistance of the sample, and multiply this by its area to get the *measured* specific resistance,

$$\rho_M \equiv \frac{V_{\text{meas}}}{I_{\text{src}}} A. \quad (6.5)$$

Ideally this ρ_M should equal the specific resistance, ρ_c , of the sample, but this

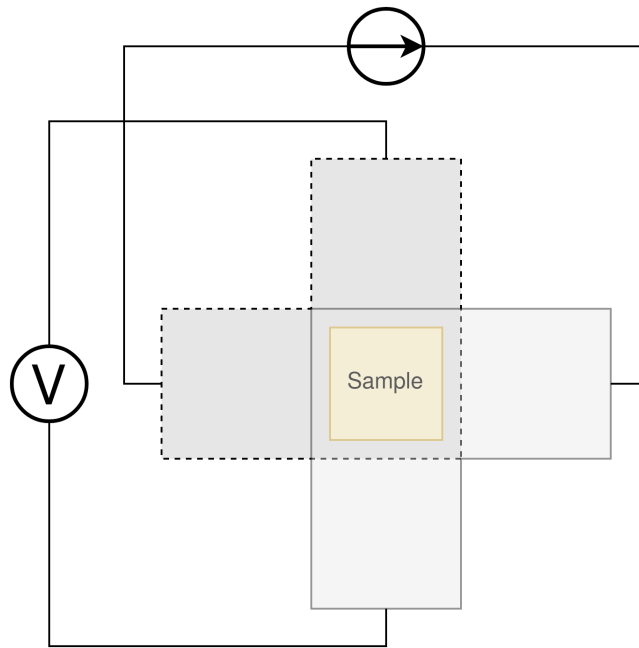


Figure 6.5: Illustration of a CBKR setup, shown are two L-shaped electrodes with a sample located in between. The electrodes are not in direct contact with each other. A current is driven from one of the legs of an L, through the sample, through the opposing leg of the other L. Meanwhile the resulting voltage is measured along the remaining legs. Also shown is a misalignment between the edges of the sample and the edges of the electrodes, this should ideally be small.

relies on some assumptions that will be checked next.

The beauty of the chosen geometry is that the measured voltage can closely resemble the average voltage over the sample. Sadly, this might not always be the case, especially not if currents flow *around* the sample due to misalignment. This is illustrated in Figure 6.6, showing simulated voltage fields around a significantly misaligned sample.

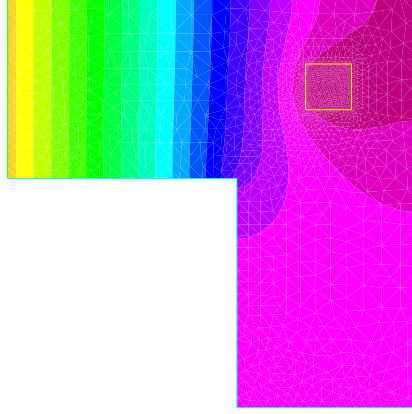


Figure 6.6: Simulated voltage field in a heavily misaligned square sample, current flows into the left leg while the bottom leg measures the voltage. For simplicity the bottom electrode is modeled as an isopotential. Simulations were performed using FreeFem++ [9]. Note that the average voltage in the sample does not match the average voltage along the measurement leg.

This effect was modeled by Schreyer and Saraswat [14], defining the measured contact resistivity ρ_M as the product of measured resistance and sample area, their result can be expressed as

$$\frac{\rho_M}{\rho_c} = 1 + \underbrace{\frac{4}{3} \frac{\delta^2}{W_x W_y} \frac{A}{L_t^2} \left[1 + \frac{\delta}{2(W_x - \delta)} \right]}_{C_g}. \quad (6.6)$$

Here δ is the sample misalignment, and W_x and W_y are the thicknesses of the voltage measurement and current driving legs. The second term in Equation 6.6 is here referred to as the geometric correction factor, or C_g . Ideally C_g is small, so that $\rho_M \approx \rho_c$, this can be realized by using small samples, small misalignments, and highly conductive electrodes. Luckily C_g can easily be estimated.

Taking $\rho_c \approx 10 \text{ m}\Omega\text{cm}^2$ as a lower bound, and suppose using pieces of household aluminium foil for contacts ($R_\square \approx 3 \text{ m}\Omega_\square$, measured with a four-point probe), this gives a worst case (i.e. shortest) transfer length of around 2 cm. For easy measurements, the needed samples should not be much smaller than a squared cm, otherwise they will be difficult to cleave and handle with tweezers. By cutting the foil carefully, electrodes can be made with an estimated

misalignment of around one mm. Substitution yields a C_g on the order of magnitude of a few thousandths, indicating that geometric effects will not be significant in this setup.

In contrast to TLM and the C&S method, no patterning and etching steps are required by the CBKR method, making it a viable option for ZnO:Al samples. Still, there are some practical drawbacks to this method regarding the fabrication of test structures. In practice it can be difficult to cleave samples to specified dimensions, so that electrodes need to be custom made for each sample piece to reduce misalignment. Additionally, making sure that there are no shorts between the flimsy pieces of aluminium foil can be challenging. Experience shows that strategically placed pieces of insulating tape can help, but in the end eyebrows will probably be raised when reading “we sandwiched the sample between some household foil and duct tape, and it just appeared to work” in the methods section of any report. Despite these drawbacks, by working carefully it is possible to make these structures from aluminium foil. Due to its compatibility with the ZnO:Al samples, the CBKR method can be used as a good sanity check for any new measurements of these samples.

6.2.4 Pin to plate

The challenges of measuring contact resistivities of ZnO:Al films were known at the start of this project, previous experience showed that reliable etching of this material is difficult, making TLM and the C&S method impractical. The approach that had been used to far was to clamp samples between a copper plate and some of the probe pins of the already available four point probe setup, as illustrated in Figure 6.7. One of the probe pins would be used to drive a current to the plate, while another pin would be used to measure the voltage across the sample. The copper plate would serve as both a current driving electrode and a reference voltage since, due to its high conductivity, the electric fields within the plate can be assumed to be negligible.

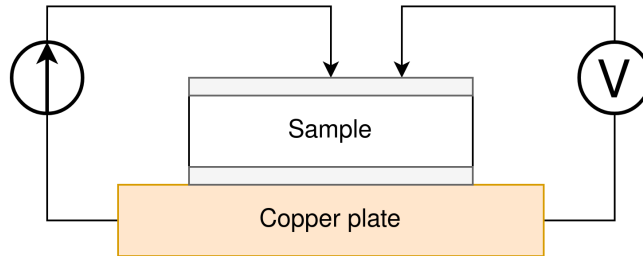


Figure 6.7: Illustration of a pin to plate measurement, featuring a copper base plate on which a silver coated sample is located. A current is driven between a pin and the base plate, while the voltage between another pin and the base plate is measured.

In essence this method is somewhat similar to the CBKR method, where a current is driven through the sample, *the* resulting voltage is measured,

and the resulting resistance is multiplied by sample area to get the specific resistivity. While in the CBKR method the average voltage along the sample is measured (neglecting geometric resistance), in the pin to plate method the relation between measured voltage and average voltage is not so clear. Due to the contacting geometry, the voltage in the top contact is highly nonuniform, so that the measured voltage can differ by orders of magnitude on a single sample, depending on where this voltage is measured. These inhomogeneities will be analyzed in detail in Chapter 7.

It quickly became clear that this method provided neither reliable nor valid results, since measurements on exactly the same sample could yield values that vary by orders of magnitude. Nonetheless, the extreme ease of measurement compared to the previously discussed measurement methods made it an interesting candidate for further investigation. If the poorly chosen probing geometry is the cause of the problematic voltage nonuniformities, then maybe a different choice of probing geometry could solve this problem.

Addressing these challenges in the pin to plate method is the goal of the rest of this thesis. The first step is to better understand the nature of current (or equivalently, voltage, by Ohm's law) inhomogeneities, this will be the goal of Chapter 7.

Chapter 7

Theory

7.1 Transfer length effects

So far, all the top-down measurement methods had to mitigate one phenomenon, transfer length effects. Consider ideal conductors used as contacts, as these form regions of equal electric potential, the potential difference between top and bottom of the sample will be equal everywhere. The driven current density will be uniform, found simply by: $J = \frac{\Delta V}{\rho_c}$. In this idealized case, contact resistivities would be trivial to measure, but in reality the driven current distributions and potential differences can be significantly inhomogeneous, as illustrated in Figure 7.1.

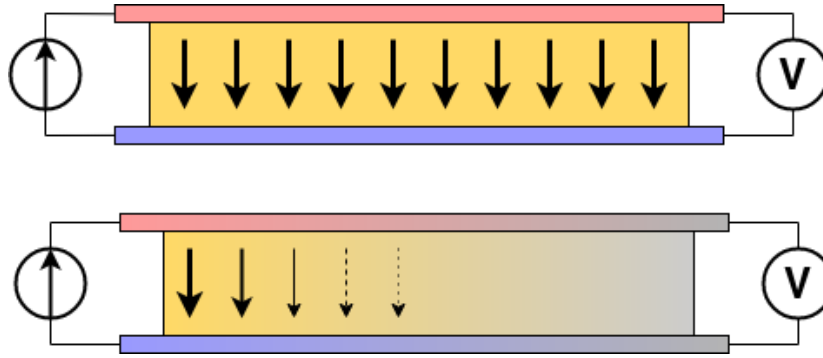


Figure 7.1: A comparison between contacting with ideally conducting electrodes (top) and electrodes with significant resistivity (bottom). Positive and negative voltages are shown as shades of red and blue in the electrodes, while the current density through the sample is depicted using arrows and shades of yellow. In the ideal case the contact voltages and current densities are uniform, while in the non-ideal case the current distribution is localized near the current injection point of the contacting electrodes.

To quantify these effects, the interaction between electrodes and sample was modeled, as illustrated in Figure 7.2.

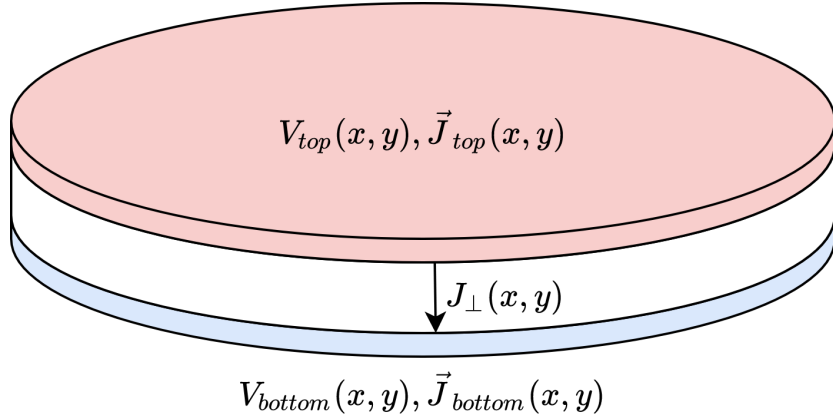


Figure 7.2: A model of a sample with two contacting electrodes. In the electrodes the current density is determined from the electrodes' conductivity and the electric fields. The current density through the sample can be determined from the stack resistivity ρ and the local potential difference between the top and bottom electrode.

7.1.1 Governing equations

In this model an arbitrary slab of sample and electrodes is considered, oriented along the x-y plane, with the z-direction defining the top and bottom of the setup. The electrodes are considered to be very thin, and relatively conductive, so that the voltage within each electrode is independent of z . Within these electrodes, the current density is determined by Ohm's law, so that

$$\vec{J}_{top} = -\sigma \nabla_{(x,y)} V_{top}(x, y), \quad (7.1)$$

and

$$\vec{J}_{bottom} = -\sigma \nabla_{(x,y)} V_{bottom}(x, y), \quad (7.2)$$

in which σ is the conductivity of the electrode material. The current density through the sample is given by

$$J_{\perp} = \frac{V_{top} - V_{bottom}}{\rho}, \quad (7.3)$$

for some specific sample resistance ρ . Consider charge conservation in any region Ω in the top electrode. This can be expressed as a sum of currents flowing into the region from other parts of the electrodes, and a current flowing into the sample:

$$0 = \int_{\Omega} \vec{J} \cdot d\vec{A} = \int_{\Omega} J_{\perp} dA + \oint_{\partial\Omega} \vec{J}_{top} \cdot \hat{n} h ds, \quad (7.4)$$

where h is the thickness of the electrode. Substitution of the current densities followed by application of the divergence theorem yields

$$0 = \int_{\Omega} \frac{1}{\rho} (V_{top} - V_{bottom}) dA - \int_{\Omega} \sigma h \nabla_{(x,y)}^2 V_{top} dA. \quad (7.5)$$

A derivation for the bottom equation gives the same result, except the sign of the J_\perp contribution is switched

$$0 = \int_{\Omega} \frac{1}{\rho} (V_{top} - V_{bottom}) dA + \int_{\Omega} \sigma h \nabla_{(x,y)}^2 V_{bottom} dA. \quad (7.6)$$

Adding the two together, and letting $\phi \equiv V_{top} - V_{bottom}$, one gets

$$0 = \int_{\Omega} -\sigma h \nabla_{(x,y)}^2 \phi + \frac{\phi}{\rho} dA. \quad (7.7)$$

As the choice of Ω was arbitrary, the integrand must vanish almost everywhere, so that

$$\nabla^2 \phi = \frac{1}{\sigma h \rho} \phi = \frac{R_{\square}}{\rho} \phi, \quad (7.8)$$

where $\frac{1}{\sigma h}$ is recognized as the sheet resistance R_{\square} .

No PDE is complete without appropriate boundary conditions, in this work Neumann boundary conditions are considered, as these describe four-point probing setups the best: a current distribution is driven along some part of the domain boundary, and some resulting potential difference is measured. In dimensionless form, the equation can be written as

$$\tilde{\nabla}^2 \phi = \left(\frac{L}{L_t} \right)^2 \phi \equiv k^2 \phi, \quad (7.9)$$

where L is the characteristic dimension of the sample, and $L_t \equiv \sqrt{\frac{\rho}{R_{\square}}}$ is the familiar transfer length, and the dimensionless Laplacian is given by $\tilde{\nabla}^2 = \frac{1}{L^2} \nabla^2$. In following sections the tilde on the Laplacian will be omitted, so that the dimensionless form of the PDE is given by

$$\nabla^2 \phi = k^2 \phi, \quad \text{Contact} \quad (7.10)$$

$$\nabla \phi \cdot \hat{n} = f \quad \text{Contact edge.} \quad (7.11)$$

7.1.2 Uniqueness of solutions

Before solving the derived equations, let's first verify that their solutions are well-behaved, offering only unique solutions. To show this, consider two solutions, ϕ_1 and ϕ_2 and let $\hat{\phi} \equiv \phi_1 - \phi_2$. The goal will be to show that the PDE and boundary conditions force ϕ to vanish. Linearity shows that $\hat{\phi}$ must obey

$$\nabla^2 \hat{\phi} = k^2 \hat{\phi}, \quad \Omega \quad (7.12)$$

$$\nabla \hat{\phi} \cdot \hat{n} = 0 \quad \partial\Omega. \quad (7.13)$$

Now consider the following integral,

$$\int_{\Omega} \nabla \cdot (\hat{\phi} \nabla \hat{\phi}) dx = \oint_{\partial\Omega} \hat{\phi} \nabla \hat{\phi} \cdot d\vec{A} \stackrel{\text{B.C.}}{=} 0, \quad (7.14)$$

apply the chain rule

$$0 = \int_{\Omega} \nabla \cdot (\hat{\phi} \nabla \hat{\phi}) dx = \int_{\Omega} \hat{\phi} \nabla^2 \hat{\phi} + \nabla \hat{\phi} \cdot \nabla \hat{\phi} dx, \quad (7.15)$$

and apply the PDE to clear the $\nabla^2 \hat{\phi}$ term,

$$0 = \int_{\Omega} k^2 \hat{\phi}^2 + |\nabla \hat{\phi}|^2 dx. \quad (7.16)$$

Since neither term inside the integral can be negative, this implies that $\hat{\phi} = 0$. This proves that solutions of Equations 7.10 and 7.11 are indeed unique.

7.1.3 Influence of transfer length

Now, let's apply this model to a few practical situations, starting with a pin to plate measurement. For simplicity, the samples are modeled as circular with radius 1, excluding the origin. Through an appropriate choice of k the solutions can describe any arbitrary combination of sample radius, contact resistivity and sheet resistance. As all currents are contained in the sample, the current density must vanish at the boundary, so that $\phi'(1) = 0$. The origin is excluded from the domain, so that a current source can be located here. In experimental conditions the total supplied current, I , is known. In this model however the average potential drop, $\bar{\phi}$, is specified, so that

$$\bar{\phi} = \frac{\int_{\Omega} \phi dA}{\int_{\Omega} dA} = \frac{2\pi}{\pi R^2} \int_0^1 r \phi(r) dr = 2 \int_0^1 r \phi(r) dr. \quad (7.17)$$

Since we're interested in deviations from the average potential, the average potential is fixed at a dimensionless value of 1. In the adopted cylindrical coordinates, the PDE can be expressed as

$$r^2 \phi''(r) + r \phi'(r) - r^2 k^2 \phi(r) = 0, \quad (7.18)$$

which is known as the modified Bessel equation. This modified Bessel function has solutions:

$$\phi(r) = A I_0(kr) + B K_0(kr), \quad (7.19)$$

in which A and B are integration constants and I_0 and K_0 are modified Bessel functions of the first and second kind [2]. By applying the boundary and integral conditions the integration constants can be found. These steps are omitted here, as it is mostly textbook linear algebra. In a simpler 1D cartesian system, the PDE reduces to $\phi'' = k^2 \phi$, which was solved with a similar boundary and integral condition. The solutions for both geometries and varying k are shown in Figure 7.3.

Figure 7.3 clearly shows the impact of the transfer length on the homogeneity of the current distribution, short transfer lengths (compared to sample dimensions) result in very inhomogeneous current distributions. Additionally, when compared at similar transfer lengths, the cylindrical solutions are much less homogeneous than the cartesian ones.

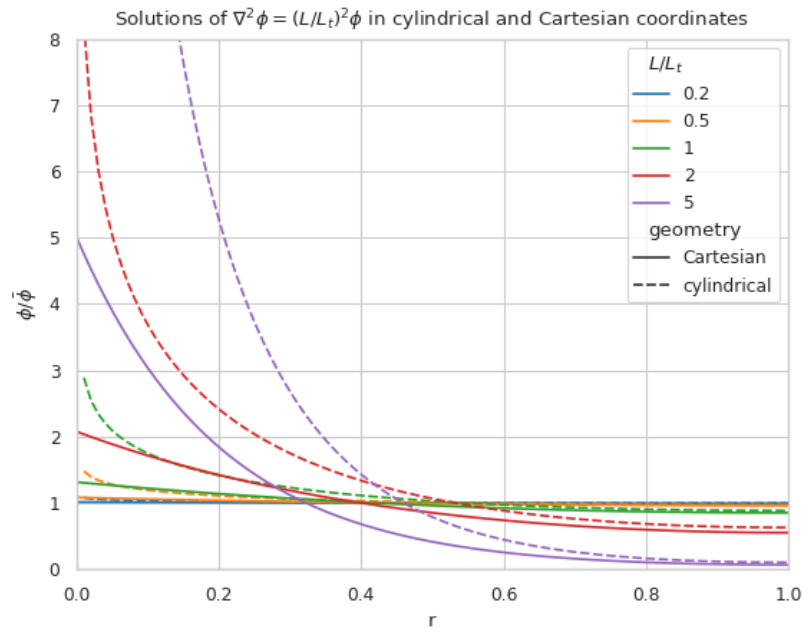


Figure 7.3: A comparison of solutions for ϕ on $(0, 1]$ in Cartesian and cylindrical coordinates, for varying $k \equiv \frac{L}{L_t}$. With boundary condition $\phi'(1) = 0$ and integral condition $\bar{\phi} = 1$. Note that the cylindrical solutions have much steeper gradients than the Cartesian ones, and that the homogeneity of the current distribution depends strongly on k , with large k leading to very inhomogeneous currents.

7.2 Idea: reduce effective sample dimensions

Suppose you were to conduct a four-point probing experiment in either the linear or circular geometry mentioned in the previous section. You drive a current through the sample, and measure some potential difference between the top and bottom of the sample, ϕ_M . You have some freedom in choosing your geometry, which one should give the best results?

To answer this question, it is useful to first estimate L_t for the samples of interest. As the current distribution is least homogeneous for small L_t , it is safest to underestimate it by using large sheet resistivities and low stack resistivities. While the stack resistivity is of course not known before the measurements, the lowest order of magnitude of ρ was estimated at $10 \text{ m}\Omega\text{cm}^2$, while for the used AZO films, $R_{sq} \approx 100 \Omega$ is not uncommon, in this case the transfer length is on the order of 0.1 mm . **QUESTION: is meer toelichting nodig?**

In practice, we'd like to be able to work with samples with dimensions of at least a few mm, not just because these are easier to handle, but because these can be easily be prepared by hand-cleaving a bigger sample piece. In these cases k would be significantly larger than 1, so the majority of current will be driven only through a small part of the sample near the current drive electrode.

The goal now is to reduce k through some means, in the ideal limiting case $k = 0$, but how close is close enough? In Figure 7.4, the normalized (with respect to the average) value of ϕ is shown at the extremes of a sample for different k , the black horizontal line indicates 99%. This shows that, in order to measure the average potential to within a percent relative error, k has to be around 0.25 or lower.

To realize this goal of decreasing $\frac{L}{L_t}$, two separate approaches are combined. The first is to increase L_t by making the contacting layers more conductive, this is achieved by depositing 300 nm of silver by e-beam evaporation. This increases L_t to approximately a few millimeters. **QUESTION: meer toelichting nodig?**

The second approach is to effectively reduce L by controlling the probe geometry. At first glance, L appears to be determined by the sample size, a current is driven through some point, and this current cannot flow out of the sample, represented in the boundary condition $\phi'(L) = 0$. An obvious option to reduce L could be to simply cut smaller samples, but in the millimeter range this is difficult, especially when areas need to be accurately determined. Working with tiny samples, while perfectly fine in theory, is undesired in practice, so can we decrease L in bigger samples? The answer is yes! The trick lies in the nature of the boundary condition, it is only required that $\phi'(L) = 0$, but does this imply that the sample is contained in the $0 < x < L$ range? Not necessarily. As an example, consider the one dimensional case: $\phi''(x) = k^2\phi(x)$ on $(0, 1)$. Now instead of applying a zero flux condition at any domain edge, simply consider solutions that are symmetric around $x = \frac{1}{2}$. These can easily be constructed from the solutions, $\phi_k(x)$, as

$$\phi_{k,\text{sym}}(x) = \frac{1}{2}(\phi_k(x) + \phi_k(1-x)). \quad (7.20)$$

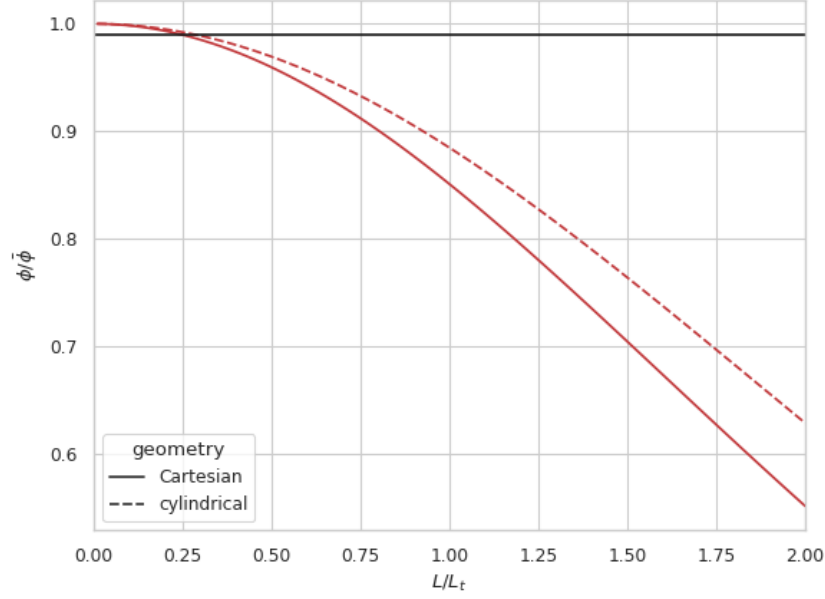


Figure 7.4: $\frac{\phi_M}{\bar{\phi}}$ at the edge of the sample, as function of $\frac{L}{L_t}$. For small $\frac{L}{L_t}$ the potential measured at the edge very closely resembles the average potential.

These solutions correspond to a current being injected through two separate contacts, located at $x = 0$ and $x = 1$.

Symmetric solutions are shown in Figure 7.5, it is clear that now $\phi'(\frac{1}{2}) = 0$. Notice the similarity between the solutions as shown in Figure 7.3 and the left half of Figure 7.5, they are the same!

Okay, so we changed the boundary conditions a bit and now we're getting symmetric solutions, what's the deal? The essential difference between the two boundary conditions is that in the first case the $\phi'(L) = 0$ condition was enforced by the samples' size. In this new one, the $\phi'(L) = 0$ condition is enforced by *where* we put our contacts, giving us freedom in choosing L ourselves! This idea is illustrated in Figure 7.6, where a current is driven through a sample using a grid of regularly spaced electrodes. Halfway each pair of electrodes, we recognize the familiar $\phi' = 0$ condition. The nonuniformities in the applied voltage are now determined by k , as indicated.

By using a regular grid of electrodes with spacing $L \ll L_t$, we can then minimize the measurement errors. In the next chapters, the actual implementation and validation of this method are discussed.

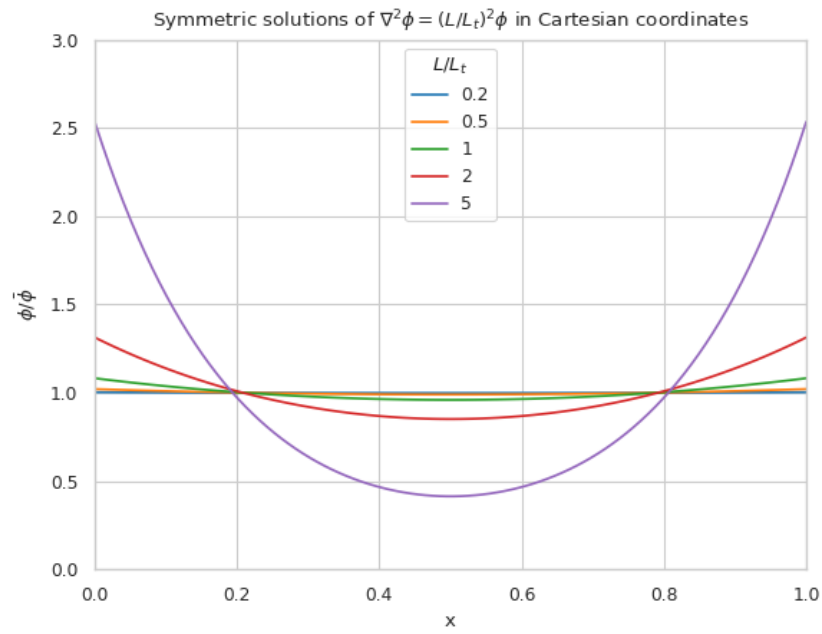


Figure 7.5: Symmetric solutions to Equation 7.10 in a 1D Cartesian geometry. Note that $\phi' = 0$ halfway between the two contacts, in this case the boundary conditions are imposed through the contact spacing, not through the total dimensions of the sample.

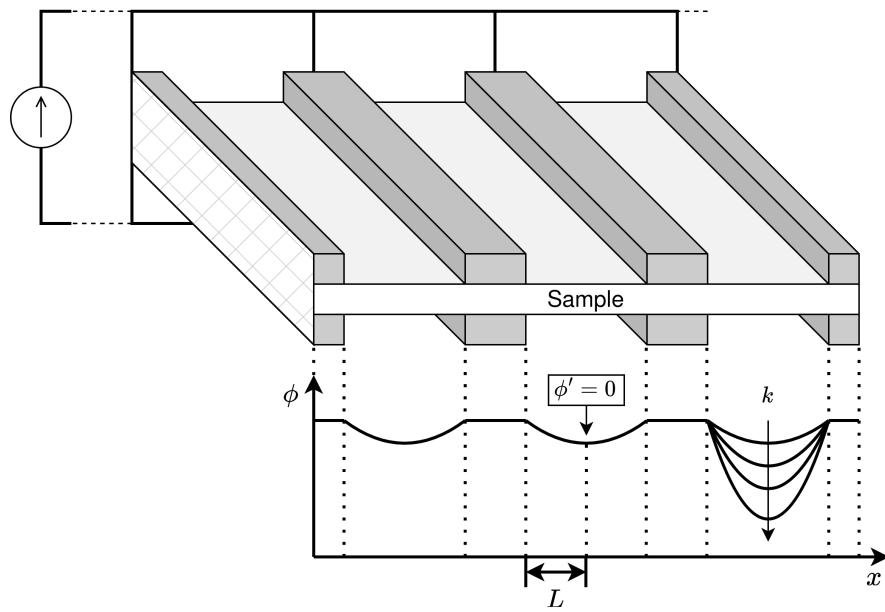


Figure 7.6: Illustration of a sample contacted by a grid of electrodes, shown below is a plot of the resulting potential as function of position. Indicated are the $\phi' = 0$ boundary condition and the effect of k on the voltage uniformity.

Chapter 8

New approach

This approach was realized using custom made printed circuit boards (PCBs), as shown in Figure 8.1. The PCBs feature a pad of regularly spaced copper lines, covering an area of 15 by 15 mm². The copper lines are alternately connected to either of the shown pins, so that they resemble interleaved combs. To perform a measurement, a sample is clamped between two such PCBs, and a current is driven between two combs on alternate sides of the sample, while the other combs are used to measure the resulting potential across the sample in a four-terminal configuration. The used copper lines were 0.6 mm wide and spaced 0.3 mm apart, with this spacing and a sample spreading length on the order of half a cm, the requirement that $\frac{L}{L_t} < 0.25$ is easily met, so that the current distribution can be considered homogeneous.

Practically, the measurements come down to the following steps:

1. Create samples that:
 - Have a spreading length significantly larger than the distance between the fingers of the PCBs to be used. Cover with silver if necessary.
 - Are homogeneous, this might not be the case when deposited films wrap around the samples.
 - Feature no edge deposited conductive films, it is recommended to cleave off the edges of the samples after silver deposition.
 - Have an accurately known surface area, A , in this work this was achieved with a computer vision method, which will be discussed later.
 - Fit on the 15 mm by 15 mm measurement pads of the PCBs.
2. Set up the resistance measurement system:
 - Use a sourcemeter in a four-terminal sensing configuration, in this work a Keithley 2400 was used.
 - Connect the current source terminals of the sourcemeter to “combs” on the two separate PCBs.
 - Connect the voltage measurement terminals to the remaining combs.
3. Clamp the sample between the PCBs
 - Make sure that the sample is located on the pads, and does not shift before measuring.
 - Use the alignment holes of the PCBs for consistent alignment.
 - Apply an evenly distributed pressure to the sample, this can be achieved with a glue clamp.
4. Perform a standard four-terminal resistance measurement, yielding resistance R .
5. Calculate the specific resistivity $\rho_s = R \cdot A$.

The interpretation of the measured stack resistivity depends on the used samples, as in this work symmetric samples were used, the stack resistivity must be larger than twice the interfacial resistivity of the AZO-Si interface. In this case an upper bound on contact resistivity can be given as $\rho_c < \frac{1}{2}\rho_s$.

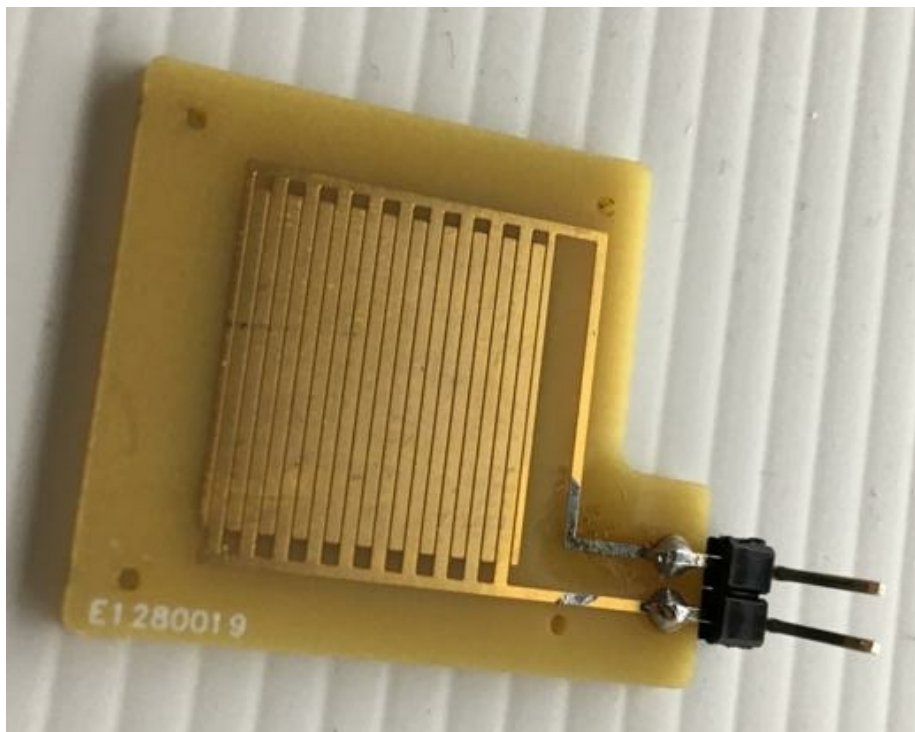


Figure 8.1: An image of a used PCB, shown are two interleaved comb-shaped copper contacts, these can be connected to measurement equipment using the two header pins. The four holes can be used to systematically align two PCBs using a pin.

Chapter 9

Characterization of measurement method

So far the case for PCB measurements has boiled down on purely theoretical arguments, in the following chapters the measurement method will be experimentally characterized. The characterization will focus on two desired properties of the new measurement: reliability and validity. A measurement method is reliable when it is reproducible, yielding the same results on each measurement. Reliability by itself is not enough though, simply because observations being close to each other does not imply that they are close to the *correct* value. A measurement is called valid if its results actually resemble what is **intended** to be measured. For a good measurement system these two qualities obviously go hand in hand.

While the reliability often refers to repeated measurements under the exact same conditions, this strict definition is not very useful when considering the PCB measurements, as the goal is to reliably measure the contact resistivity **without** regard to some sample handling details. For context, the initial measurement system (TODO footnote: detail pin to plate) proved quite reliable when a single sample was contacted and stayed fixed between measurements. Problems started appearing however, as soon as this sample was contacted with different pins, in slightly different locations, rotated a bit, or a different sample piece was used. The estimated contact resistivities varied unpredictably when even slight, to the user practically unnoticeable, changes were made to the setup. The goal here is not to be reliable under strict control of all influencing factors, but to be reliable in a somewhat chaotic environment, one in which the user can choose not to care about the exact shape and contacting points of their samples, and still get *reliable* results. For this reason, the term reliability is used in a looser sense in this work: a measurement is considered reliable when it yields similar (enough) results in a range of realistic usage scenarios.

More practically speaking, these “realistic usage scenarios” should at least include different contacting conditions, like where the sample is located and in

which orientation, but also simply using another sample of differing dimensions. These reliability experiments were done by varying exactly the mentioned conditions and measuring if these influence the measurement, this will be discussed in more detail in following sections.

To check the validity of the measurement, a reference measurement is needed. Ideally a sample with a well known specific resistance could be used, but these were not available. Another option is to take a sample, measure the specific resistance through some other means, and then compare the results with the new method. This concurrent validity test was chosen, in which the novel method was compared to a cross bridge kelvin resistor (CBKR). The choice for a CBRK test was made since it can handle the same type of samples that the PCBs can. The needed patterning for Cox & Strack and other methods would imply the need to make separate samples, process them differently, and just hope that they have the same specific resistance. A CBRK allows for measurements on the exact same samples as on the PCBs, without any alterations, making it fit for a direct comparison of measurement methods. The used CBRK setup will be discussed in more detail in Section 10.2.

Chapter 10

Results

10.1 Reliability

Ideally the PCB method should yield the same contact resistivities, regardless of

- Sample orientation,
- Sample position,
- Sample shape.

These assumptions were checked, starting with the sample orientation. Here the contact resistivity was measured for two cases, in the “long” case the long edge of the sample was aligned parallel to the fingers of the PCBs, while in the “short” case the short edge was aligned parallel to the fingers. This was done for two symmetric samples:

1. pSi substrate with r48 AZO annealed at 400C, measuring approx 4.5 mm by 6.5 mm.
2. 130 Ω n+ Si with r48 AZO annealed at 400C, measuring approx 6.5 mm by 9.0 mm.

The results are shown in Figure 10.1. For the pSi sample, the results are quite consistent, while for the n+ Si sample there is more spreading in the measurements. This can be explained by the pSi sample having a larger contact resistivity than the n+ Si sample, and thus a larger spreading length, this sample also happened to have smaller dimensions, so that overall the current distribution can be expected to be more homogeneous. Overall, the measurement seems most repeatable in the “short” configuration.

Next the location of the sample on the PCB was varied for a few samples. The samples were located at all four extreme corners of the PCB pad and at the center. Figure 10.2 shows the measured results for each of the tested

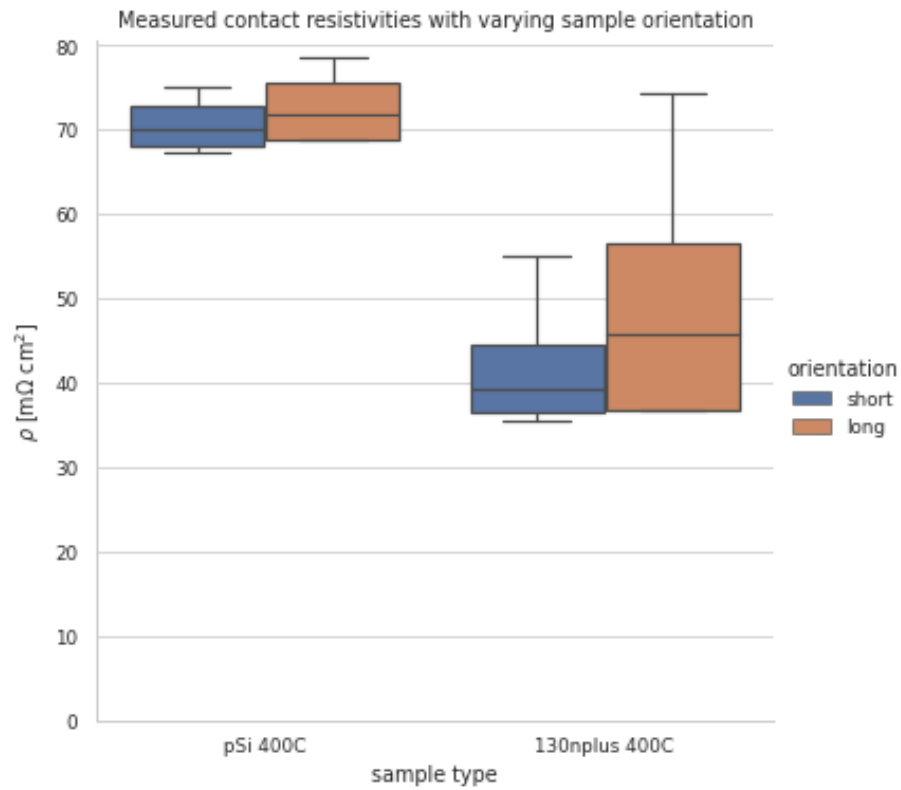


Figure 10.1: Measured contact resistivities with varying orientation. Two different samples were used, for which the contact resistivity was measured in different orientations. In the “short” cases, when the short side of the sample lies parallel to the PCB’s fingers, the measurements are most reliable.

samples, note the logarithmic vertical axis. This shows that the measurement is typically reliable on a per-sample basis. There are some clear deviations between pieces cut out of the same wafer, while these should all have the same contact resistivities, Figure 10.2 shows that this is not the case. A possible cause for this is backside deposition of Al_2O_3 resulting in nonuniform samples, which was observed to occur by TEM.

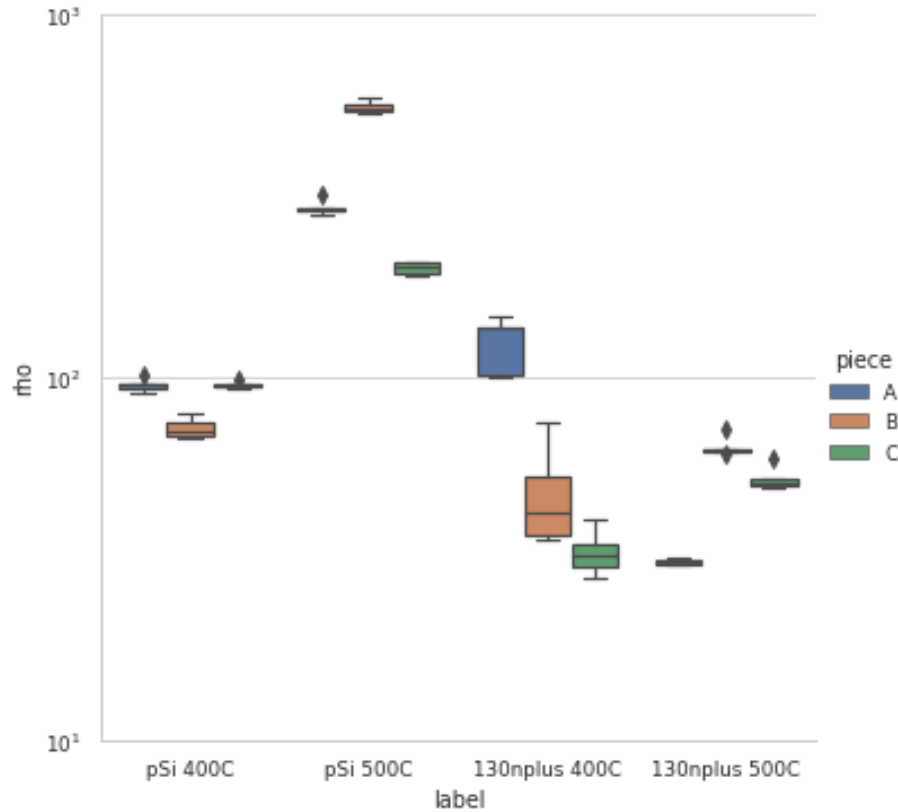


Figure 10.2: Measured contact resistivities of different pieces of different samples, the spread between measurements on different pieces are often larger than the spread within the pieces. The pieces are labeled in order of their overall size, A being the largest within each category.

10.2 Validity: Cross Bridge Kelvin Resistor comparison

Finally the PCB method was cross-validated with a Cross Bridge Kelvin Resistor (CBKR) setup which was carefully crafted from pieces of aluminium foil. While this alternate method is difficult and time consuming to perform, it provides a good sanity check for the PCB method. To do this, two L-shaped pieces of aluminium foil were cut, with the widths of the legs matching the dimensions of

the samples. These contacting pads were made for each specific sample. Then the sample was clamped between the pieces of foil, while pieces of insulating tape ensured that no shorts could occur between the contacting pads. Two opposing “legs” were used to drive a current, while the potential difference was measured between the others, again in a four-point probe configuration. Several samples were used, for which the contact resistivity was measured multiple times with the PCB method and the CBKR method, Figure 10.3 shows that the results correlate strongly, here the error bars show the minimal and maximal values for each measurement.

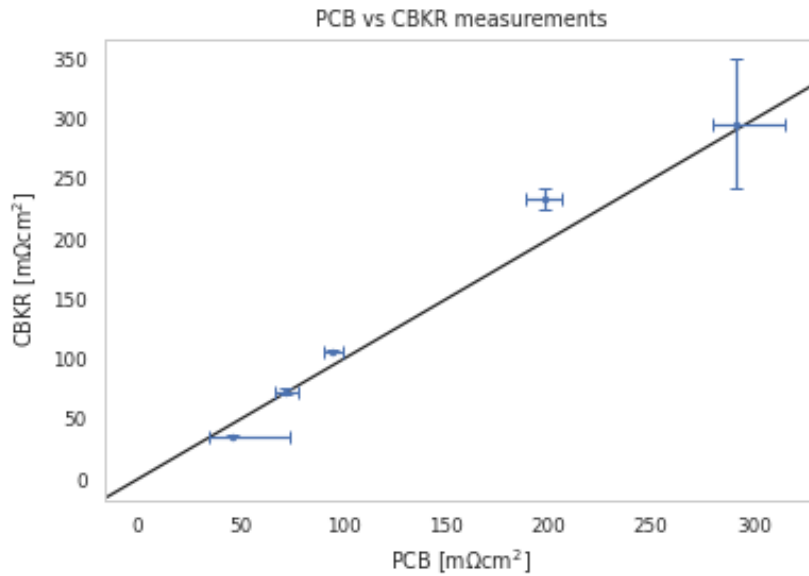


Figure 10.3: Comparison between PCB measurements and and CBKR measurements on a set of samples, the error bars indicate the minimum and maximum of the measured values. Ideally the measurements should match exactly, which is indicated by the black line.

Chapter 11

Conclusion

A method for easy contact resistivity measurements on laterally uniform samples was developed. This was achieved by contacting samples with custom made printed circuit boards, featuring interleaved comb-like copper contacts, which are used to drive a uniform current distribution through a sample. In contrast to the Cox & Strack and transmission line methods, which involve delicate sample patterning steps, the method developed here only requires uniform conductive contacting layers. This is especially important for ZnO:Al samples, since controlled etching of these layers is known to be difficult, rendering TLM and the C&S method impractical. In essence, the new method shows similarities to the CBKR method, both methods use a four terminal approach, and both aim to eliminate inhomogeneous currents by electrode design. In contrast to the CBKR method, in which the electrode dimensions need to match the sample dimensions, the PCBs used in the new method enable a rapid reuse of the same testing structure for samples of different dimensions.

Bibliography

- [1] PERCspective: perspective for PERC in tandems with perovskite. <https://projecten.topsectorenergie.nl/projecten/percspective-perspective-for-perc-in-tandems-with-perovskite-33521>, <https://projecten.topsectorenergie.nl/projecten/percspective-perspective-for-perc-in-tandems-with-perovskite-33521>.
- [2] M. Abramowitz and I. A. Stegun. *Handbook of Mathematical Functions with Formulas, Graphs, and Mathematical Tables*. Dover, New York, ninth dover printing, tenth gpo printing edition, 1964.
- [3] M. Ahmad, T. Ganguli, S. Patil, S. Major, Y. G. K. Patro, and B. M. Arora. Determination of contact resistivity by a modified Cox and Strack method in case of finite metal sheet resistance. *Solid-State Electronics*, 38(8):1437–1440, Aug. 1995.
- [4] E. Bunte, H. Zhu, J. Hupkes, and J. Owen. Novel texturing method for sputtered zinc oxide films prepared at high deposition rate from ceramic tube targets. *EPJ Photovoltaics*, page 8.
- [5] R. H. Cox and H. Strack. Ohmic contacts for GaAs devices. *Solid-State Electronics*, 10(12):1213–1218, Dec. 1967.
- [6] A. Cuevas. The Recombination Parameter J_0 . *Energy Procedia*, 55:53–62, Jan. 2014.
- [7] L. Dennis. Master thesis DGJA Loeffen (PMP).pdf, 1234.
- [8] K. C. Fong, T. C. Kho, W. Liang, T. K. Chong, M. Ernst, D. Walter, M. Stocks, E. Franklin, K. McIntosh, and A. Blakers. Optimization and Characterization of Phosphorus Diffused LPCVD Polysilicon Passivated Contacts with Low Pressure Tunnel Oxide. In *2018 IEEE 7th World Conference on Photovoltaic Energy Conversion (WCPEC) (A Joint Conference of 45th IEEE PVSC, 28th PVSEC & 34th EU PVSEC)*, pages 2002–2005, Waikoloa Village, HI, June 2018. IEEE.
- [9] F. Hecht. New development in FreeFem++. *Journal of Numerical Mathematics*, 20(3-4):251–265, 2012.

- [10] J. Hüpkes, J. I. Owen, S. E. Pust, and E. Bunte. Chemical Etching of Zinc Oxide for Thin-Film Silicon Solar Cells. *Chemphyschem*, 13(1):66–73, Jan. 2012.
- [11] B. Macco, B. W. H. van de Loo, M. Dielen, D. G. J. A. Loeffen, B. B. van Pelt, N. Phung, J. Melskens, M. A. Verheijen, and W. M. M. Kessels. Atomic-layer-deposited Al-doped zinc oxide as a passivating conductive contacting layer for n+-doped surfaces in silicon solar cells. *Solar Energy Materials and Solar Cells*, 233:111386, Dec. 2021.
- [12] B. Macco, B. W. H. van de Loo, and W. M. M. Kessels. Atomic Layer Deposition for High-Efficiency Crystalline Silicon Solar Cells. In J. Bachmann, editor, *Atomic Layer Deposition in Energy Conversion Applications*, pages 41–99. Wiley-VCH Verlag GmbH & Co. KGaA, Weinheim, Germany, Mar. 2017.
- [13] K. R. McIntosh and S. C. Baker-Finch. OPAL 2: Rapid optical simulation of silicon solar cells. In *2012 38th IEEE Photovoltaic Specialists Conference*, pages 000265–000271, Austin, TX, USA, June 2012. IEEE.
- [14] T. Schreyer and K. Saraswat. A two-dimensional analytical model of the cross-bridge Kelvin resistor. *IEEE Electron Device Letters*, 7(12):661–663, Dec. 1986.
- [15] D. Schroder and D. Meier. Solar cell contact resistance—A review. *Electron Devices, IEEE Transactions on*, 31:637–647, June 1984.
- [16] D. K. Schroder. *Semiconductor Material and Device Characterization*. John Wiley & Sons, Inc., Hoboken, NJ, USA, Apr. 2005.
- [17] K. G. Sun, Y. V. Li, D. B. Saint John, and T. N. Jackson. pH-Controlled Selective Etching of Al₂O₃ over ZnO. *ACS Applied Materials & Interfaces*, 6(10):7028–7031, May 2014.
- [18] B. W. H. van de Loo, B. Macco, J. Melskens, W. Beyer, and W. M. M. Kessels. Silicon surface passivation by transparent conductive zinc oxide. *Journal of Applied Physics*, 125(10):105305, Mar. 2019.
- [19] L. J. van der PAUW. *A METHOD OF MEASURING SPECIFIC RESISTIVITY AND HALL EFFECT OF DISCS OF ARBITRARY SHAPE*, pages 174–182. WORLD SCIENTIFIC, Mar. 1991.
- [20] M. van Rijnbach, R. J. E. Hueting, M. Stodolny, G. Janssen, J. Melskens, and J. Schmitz. On the Accuracy of the Cox–Strack Equation and Method for Contact Resistivity Determination. *IEEE Transactions on Electron Devices*, 67(4):1757–1763, Apr. 2020.